

Transient Safety Analysis of Fast Spectrum TRU Burning LWRs with Internal Blankets

Reactor Concepts

Dr. Thomas Downar
University of Michigan

In collaboration with:
Massachusetts Institute of Technology
Argonne National Laboratory

Thomas Sowinski, Federal POC
Temitope Taiwo, Technical POC

FINAL REPORT

Project Title: Transient Safety Analysis of Fast Spectrum TRU Burning LWRs with Internal Blankets

Covering Period: Final

Date of Report: January 31, 2015

Recipient: University of Michigan
2355 Bonisteel Blvd
Ann Arbor, MI 48109-2104

Contract Number: 89536

Project Number: 09-812

Principal Investigators: Thomas Downar – downar@umich.edu

Mujid Kazimi – kazimi@mit.edu

Project Objective:

The objective of this proposal was to perform a detailed transient safety analysis of the Resource-Renewable BWR (RBWR) core designs using the U.S. NRC TRACE/PARCS code system. This project involved the same joint team that has performed the RBWR design evaluation for EPRI and therefore be able to leverage that previous work. And because of their extensive experience with fast spectrum reactors and parfait core designs, ANL was also part the project team. The principal outcome of this project was the development of a state-of-the-art transient analysis capability for GENIV reactors based on Monte Carlo generated cross sections and the US NRC coupled code system TRACE/PARCS, and a state-of-the-art coupled code assessment of the transient safety performance of the RBWR.

TPOCS: Temitope Taiwo - taiwo@anl.gov

Federal POC: Thomas Sowinski – Thomas.Sowinski@nuclear.energy.gov

Collaborators: Bob Hill - bobhill@anl.gov

Table of Contents

FINAL REPORT	1
Chapter 1: Introduction.....	3
Chapter 2: Background on the RBWR	4
Chapter 3: RBWR Modeling	6
3.1 RBWR Design Features.....	6
3.2 Methods.....	6
Chapter 4: PARCS-PATHS Analysis.....	20
4.1 Single Assembly Analysis.....	20
4.2 Equilibrium Cycle Analysis - AC	21
4.3 RBWR-AC Reactivity Coefficients	23
4.4 Monte Carlo Void Coefficient Confirmation	25
4.5 Equilibrium Cycle Analysis – TB2.....	28
4.6 TB2 Reactivity Coefficients.....	29
Chapter 5: Safety and Stability Modeling Development.....	31
5.1a Critical Power Implementation	31
5.1b Post Critical Power Heat Transfer Logic Implementation	31
5.1c Fuel Thermal Conductivity Model	34
5.1d RBWR TRACE Model.....	34
5.1e RBWR PARCS Model.....	34
5.2 Coupled Steady State Simulation.....	35
Chapter 6: Safety and Stability Analysis.....	37
6.1 Safety Analysis	37
6.2 Stability Analysis	43
Chapter 7: Summary	49
7.1 PARCS/PATHS Equilibrium Cycle	49
7.2 PARCS/TRACE Transient and Stability Simulations.	49

Chapter 1: Introduction

The following report summarizes the work performed in the project “Transient Safety Analysis of Fast Spectrum TRU Burning LWRs with Internal Blankets”. The report is separated into a sequence of Chapters describing work performed on each phase of the project as identified in the original work scope:

Period 1 Year 1 10/1/11 – 3/31/12

1. Develop TRACE/PARCS systems model of RBWR-AC
2. Generate and benchmark cross section and kinetics data for RBWR-AC with SERPENT

Period 2 Year 1 4/1/12 – 9/30/12

1. Perform TRACE/PARCS equilibrium core calculation
2. Implement and benchmark tight pitch lattice CPR into TRACE
3. Develop TRACE/PARCS model for stability analysis of RBWR-AC

Period 3 Year 2 10/1/12 – 3/31/13

1. Perform TRACE/PARCS equilibrium core transient simulation of RBWR-AC Recirculation Pump Trip
2. Perform TRACE/PARCS stability analysis of RBWR-AC
3. Generate and benchmark cross section / kinetics data for RBWR-TB2 with SERPENT

Period 4 Year 2 4/1/13 – 9/30/13

1. Develop TRACE/PARCS RBWR-TB2 equilibrium core calculation with TRACE/PARCS
2. Develop TRACE/PARCS stability model of the RBWR-TB2

Period 5 Year 3 10/1/13 – 3/31/14

1. Perform TRACE/PARCS transient simulation of RBWR-TB2 Recirculation Pump Trip
2. Perform TRACE/PARCS stability analysis of the RBWR-TB2

Period 6 Year 3 4/1/14 – 9/30/14

1. Perform additional TRACE/PARCS transient simulation as necessary
2. Prepare Documentation and Final Report
3. Perform additional TRACE/PARCS transient simulation as necessary
4. Prepare Documentation and Final Report

The next chapter provides a brief overview of the RBWR core design and Chapter 3 will describe the neutronics methods developed to analyze the RBWR. Chapter 4 will then discuss the development of the equilibrium core for both the RBWR-AC and RBWR-TB2. Chapter 5 will describe the TRACE model developed for transient analysis and Chapter 6 will present the results of the transient and stability calculations. Chapter 7 will provide a summary, conclusions, and areas for future work.

Chapter 2: Background on the RBWR

Relative to the BWR (and ABWR), the RBWR core design features a tighter fuel lattice, a shorter core, a smaller coolant mass flow-rate and pressure drop, a larger exit void fraction and a less negative core void reactivity coefficient. The design of the RBWR is shown in Fig. 2-1 and some of the characteristics of the RBWR and the ABWR are compared in Table 2-1. As indicated in the Table, the RBWR has a lower coolant flow rate, higher void fraction, and less negative void coefficient compared to the ABWR.

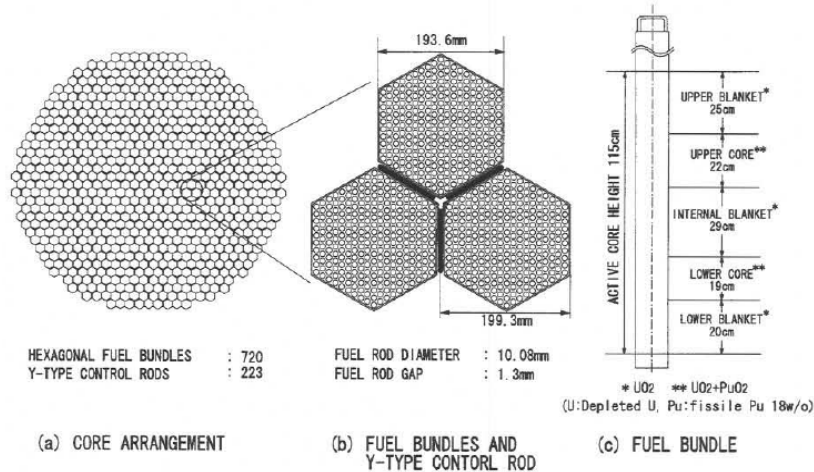


Figure 2-1. Core Design of the RBWR [1]

Table 1 Design Characteristics of the RBWR Compared to the ABWR [1]

Item	RBWR-AC	Item	ABWR
Thermal Power MWt	3926	Thermal Power MWt	3926
Electrical Power MWe	1356	Electric Power MWe	1356
No. of Fuel Bundles	720	Number of Fuel Bundles	872
Core Height mm	1200	Core Height mm	3710
Configuration for Height	Parfait		
Coolant Flow Rate kt/h	22	Coolant Flow Rate kt/h	58
Core Exit Quality %	41	Core Exit Quality %	13
Void Fraction %	60	Void Fraction %	36
Pressure Drop MPa	0.11	Core Pressure Drop MPa	0.21
HM Inventory t	131	Uranium Inventory t	151
Pu/HM in Fissile Zone w/o	18	Uranium Enrichment wt%	3.8
Pu Inventory t	8.9		
Burnup GWd/t	45	Burnup GWd/t	45
MLHGR kW/ft	14.4	MLHGR kW/ft	12
MCPR	1.3	MCPR	1.3
Void Coef. $\Delta k/k\%$ void	-2×10^{-5}	Void Coefficient $\frac{10^{-4} \Delta k/k}{\% \text{void}}$	-12×10^{-5}

The less negative void coefficient in the RBWR is because of the harder spectrum resulting from the higher void fraction and the tighter lattice. And in general fast spectrum reactors have the potential for a positive core void coefficient, primarily because the spectrum is already hard and core voiding can result in an even harder spectrum and a corresponding increase in the fast fission probability of ^{238}U and in η of the TRU isotopes. The spectrum of the RBWR is compared to the LWR and SFR (ARR) in Fig. 2. One of the principal reasons for the much harder spectrum of the RBWR is the large reduction in the Hydrogen scattering cross section at high energies which is also shown in Fig. 2-2.

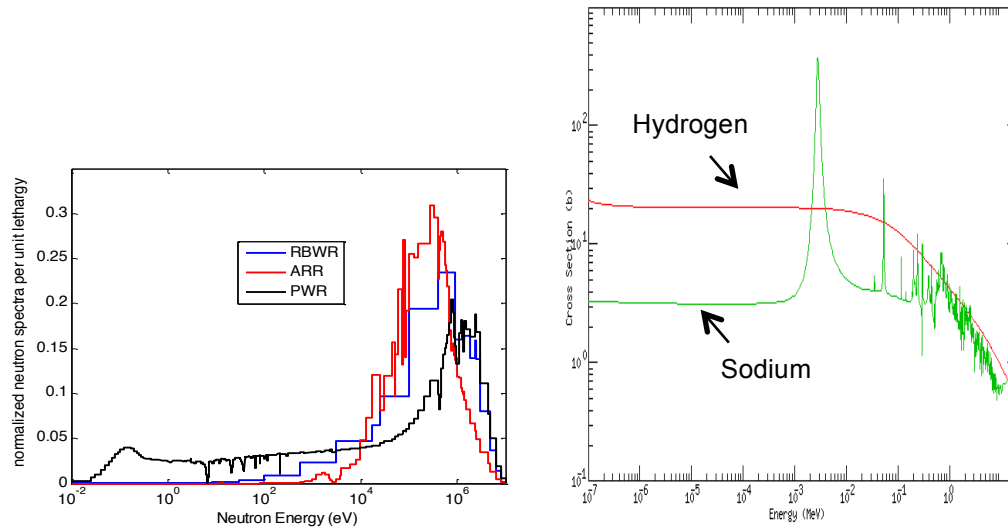


Figure 2-2. Comparison of the Spectra of the RBWR, ARR (SFR), and LWR

In order to mitigate the potential for a positive void coefficient most designs of fast spectrum cores have introduced innovative features such as large internal blanket regions in order to provide lower importance neutron sinks in the event of core voiding during a transient. The core void and power distribution of the RBWR that were calculated by the PIs using RELAP5/PARCS are shown in Fig. 2-3 [2]. As indicated the power in the internal blanket region is significantly lower than the power in the upper and lower fissile regions of the core. The positive reactivity effects of increased neutron production in the fissile regions during voiding would be mitigated by leakage of neutrons into the lower importance blanket region. There have been numerous sodium fast reactor (SFR) designs which have successfully achieved negative void coefficient values with axial blankets of natural uranium [3]. However, the designers of these reactors have pointed out that achieving a negative void coefficient with large internal blankets can lead to core designs which may be less safe because they introduce other safety issues. The focus of the work performed here was to examine the transient safety performance of the RBWR. The work built upon the PIs previous experience with the RBWR funded by EPRI and Hitachi, as well as the previous experience of the PIs with the U.S. NRC TRACE/PARCS code for LWR transient analysis.

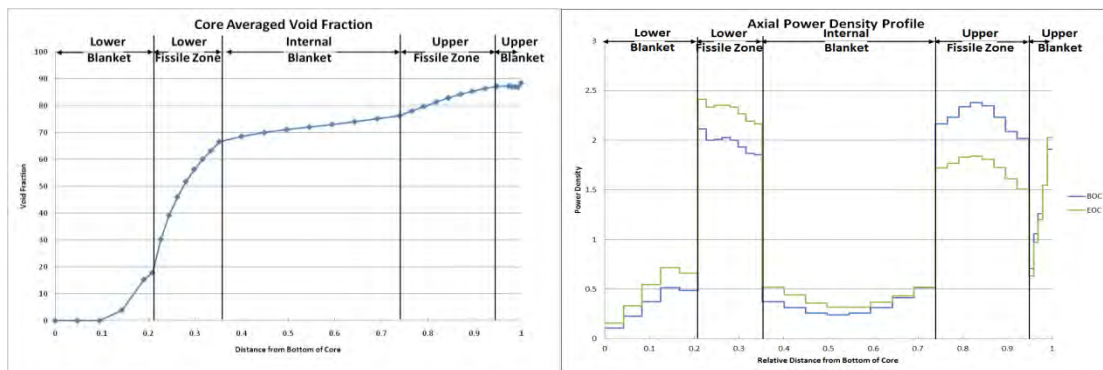


Figure 2-3. Axial Core Void and Power Distributions in the RBWR

Chapter 3: RBWR Modeling

The spectrum of the RBWR cores can be similar to that of a fast reactor or an LWR, depending on the location. The moderator density has a large impact on the spectrum, and thus on the whole analysis. Because of the axial heterogeneities in the core, there were several uncommon modeling challenges that do not factor in when analyzing standard LWR designs.

3.1 RBWR Design Features

The RBWR-AC was designed specifically to achieve a conversion ratio of 1.0 using several special design features. Each assembly is composed of alternating blanket and seed regions. There are two seed regions which are composed of enriched plutonium with an isotopic transuranic (TRU) vector. Each seed region consists of 5 different pin types of varying enrichment. Both of these regions are located between blanket zones that contain depleted uranium. The design of the RBWR can be seen in Fig. 2-1. This configuration separates the two seed regions providing a unique double-peaked power distribution as shown in Fig. 2-3. The RBWR lattice also features a high average void fraction and tight pitch lattice. The harder spectrum promotes breeding of plutonium within the blanket regions from neutrons exiting the seed regions. Another feature of the harder spectrum is the ability to burn TRU isotopes within the fuel, which reduces the amount of TRU discharged from the fuel assembly.

The RBWR-TB2 was designed to achieve a TRU fission efficiency of 45%. Fission efficiency is defined as the net decrease in TRUs divided by the total amount of fissioned heavy metal for the total fuel life. Unlike the RBWR-AC, there is no lower blanket region and a much smaller upper blanket region. The TB2 fuel rods are smaller in diameter than the AC rods, which reduces the fuel-to-moderator ratio. Each assembly contains 397 fuel rods (c.f. 271 for the RBWR-AC). The design changes from the RBWR-AC allow the RBWR-TB2 to operate to higher burnups allowing for an increased consumption rate of TRU.

The RBWR assemblies are short (~1m in height) and the 720 assemblies are arranged in a multi-batch fuel loading. This “pancake” core configuration has a significantly increased axial leakage compared to conventional LWRs. A large axial reflector (1.3m) is used at the top of the active core region to improve the overall neutron economy within the core. Because of these large axial heterogeneities, there have been limitations in using the conventional LWR analysis methods which utilize 2D lattice calculations. Instead, a new class of methods has been developed based on the generation of 3D cross sections using the Monte Carlo code Serpent. These 3D methods have proven to be especially important when developing cross section for the large axial reflector regions at the top of the core where accurate neutronics modeling is necessary to calculate safety performance parameters such as the void coefficient.

3.2 Methods

The neutronics modeling of the RBWR consists of a multi-step calculation process similar to existing LWR analysis methods. For the first step, 3D cross sections are generated for a single assembly. These cross sections are generated at all anticipated temperature and fluid conditions in the reactor and are then processed and converted into a PMAXS format which can be read by

the PARCS code. The final step involves a coupled-code simulation using the tabulated group constants to model the full core behavior. An overview of the codes used for this analysis can be seen in Fig. 3-1.

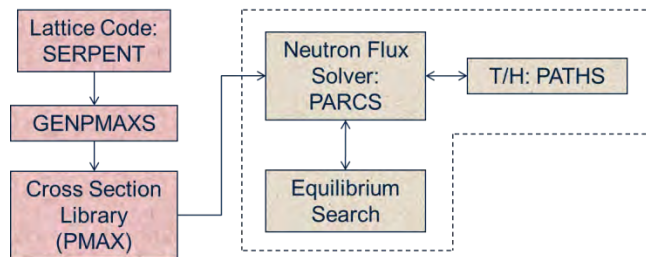


Figure 3-1. Core simulator diagram.

3.2a Cross Section Generation

Cross sections for the RBWR were created using the Monte Carlo code Serpent. The code utilizes delta tracking to accelerate the calculation while generating group-wise homogenized parameters [4]. These group constants are collapsed based on ENDF/B-VII continuous energy data. The assembly was divided into several axial levels based on the Hitachi discretization. The y-shaped control rod was collapsed so that the entire assembly fit within a single regular hexagon. Fig. 3-2 shows the Serpent lattice and axial geometry for the RBWR-AC. The different colored pins show the layout of the 5 different plutonium enrichments in the fissile regions. The RBWR-TB2 lattice (Fig. 3-3) is hexagonal pitch like the RBWR-AC lattice, but the pins are smaller and there are more pins per assembly (and only one pin type). This model was used because Serpent can only handle global boundary conditions on a single defined surface. Some simplifications were also made to the Serpent model: for example, the 5 different pin types within each seed region were homogenized into a single pin type to help reduce memory requirements. Reflective boundary conditions were applied in the radial direction, while zero incoming current conditions were applied for the top and bottom of the assemblies. The cross sections were calculated with the P1 infinite spectrum. When developing 3D Monte Carlo cross sections, the total number of particle histories is crucial in reducing the error associated with the generated group constants. Each cross section is calculated with tallies from the simulation. If the number of simulated particles is too small, the uncertainty of these tallies will be large. Increased uncertainties may lead to greater errors in the cross sections, which affect the accuracy of the nodal solution.

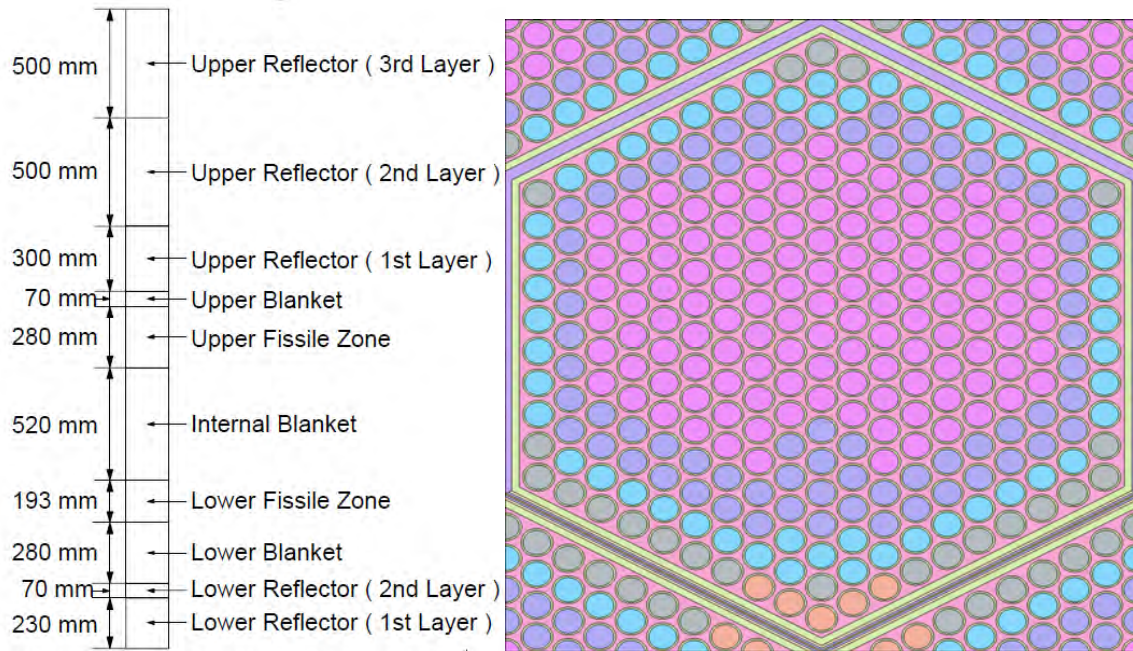


Figure 3-2. RBWR-AC axial (left) and radial (right) assembly model.

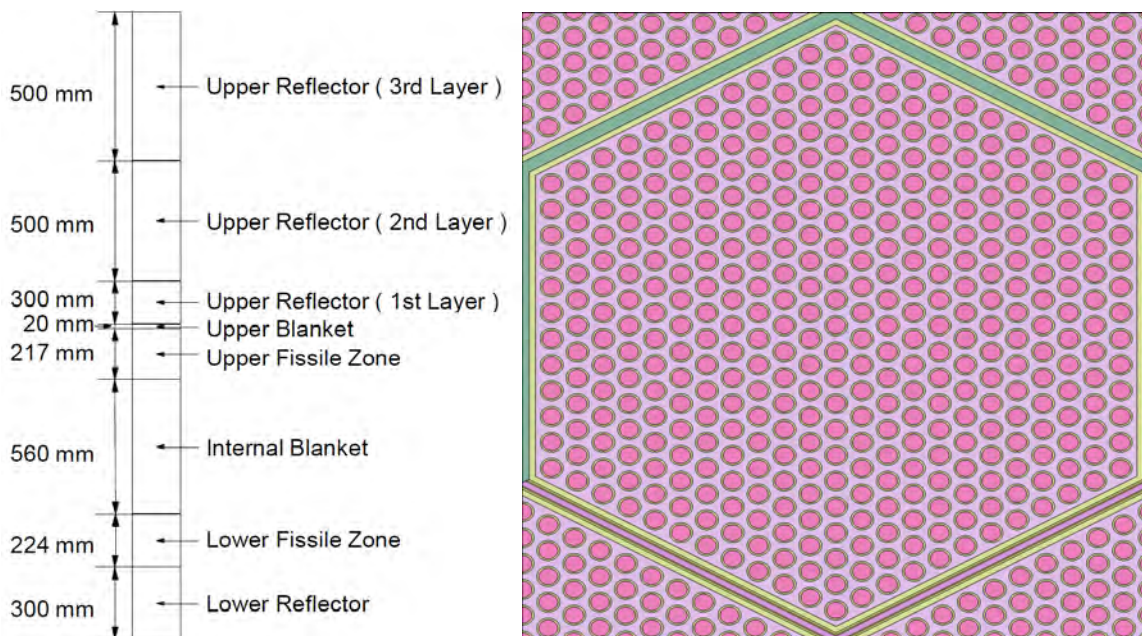


Figure 3-3. RBWR-TB-2 axial (left) and radial (right) assembly model.

A history and branching scheme was developed based on previous experience modeling the RBWR [5]. However, the use of 3D cross sections has required changes in the typical scheme for generating branch conditions. When performing 2D lattice calculations, individual conditions are perturbed including fuel temperature, coolant void, control rod insertion, etc. For 3D assembly calculations, the conditions at multiple positions in the core must be changed simultaneously. A

small study was performed at Brookhaven National Lab (BNL) that illustrated the effect of the spectrum when perturbing individual regions as opposed to all regions simultaneously (integral method) [6]. A comparison of the spectrum for the upper fissile region is shown in Fig. 3-4. From this analysis, significant changes in the spectrum were observed when perturbing the coolant void for individual nodes. The same study was performed for the spectrum when perturbing the fuel temperature and showed minimal changes. Additional information on the spectral effect of perturbing coolant density and fuel temperature for various regions can be found in Appendix B. Therefore a system was devised to perturb the entire axial void distribution for branching calculations to maintain a physical distribution within the assembly. The method involved generating an initial set of 2D Serpent cross sections which were used in a single assembly PARCS simulation coupled with PATHS to generate an initial guess for the void distribution. PATHS is a drift flux thermal-hydraulics code that solves the mass, momentum and energy equations. This void distribution was then placed within a 3D Serpent calculation to generate a set of 3D Serpent cross sections. Using these group constants, a second set of coupled PARCS/PATHS simulations, for a single assembly, were performed to generate the final void distribution to be used for each branch and history. This technique provides a coolant void distribution that is closer to that of the physical system compared to a uniform distribution.

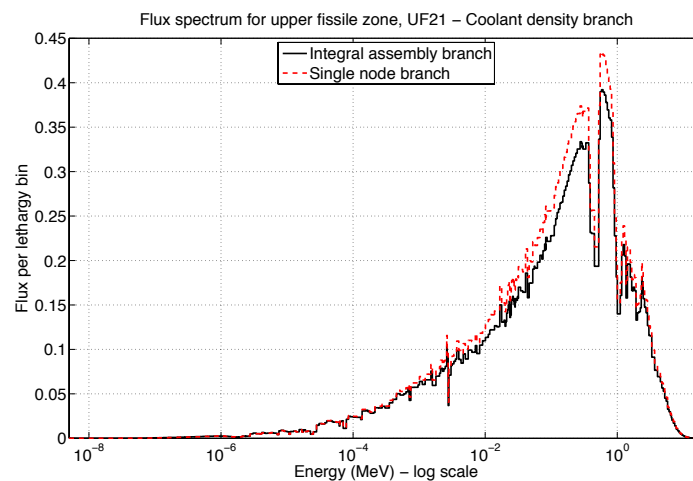


Figure 3-4. Flux spectrum for upper fissile zone.⁵

Using the generated void distributions, a set of 4 histories and 10 branches were used to specify the core conditions for the cross section calculations. The branches include: a reference condition, a low uniform fuel temperature perturbation, a high uniform fuel temperature perturbation, 2 lower flow perturbations, 2 higher flow perturbations, and one cross branch with a control rod inserted at high moderator density. The four histories include: a reference condition, low flow perturbation, high flow perturbation and a case with the control rod fully inserted. Tables 5-1 through 5-4 show the cross section history and branch structure for the AC and TB2. A control rod state of 0 means the control is withdrawn (graphite follower in gap) and a control rod state of 1 means the rod is inserted (absorber in gap).

Table 5-1
RBWR-AC History Structure

History	Control Rod State	Core Average Moderator Density (g/cc)	Corresponding Void Fraction (%)	Fuel Temperature (K) (blanket/fissile)
1	0	0.33402	58	600/900
2	0	0.25845	68	600/900
3	0	0.50281	33	600/900
4	1	0.33402	58	600/900

Table 5-2
RBWR-AC Cross Section Branch Structure

Branches	Index	Control Rod State	Core Average Moderator Density (g/cc)	Corresponding Void Fraction (%)	Fuel Temperature (K) (blanket/fissile)
RE	1	0	0.33402	58	600/900
CR	2	1	0.33402	58	600/900
DC	3	0	0.00001	100	600/900
DC	4	0	0.25845	68	600/900
DC	5	0	0.50281	33	600/900
DC	6	0	0.76000	0	600/900
DC	7	1	0.76000	0	600/900
TF	8	0	0.33402	58	500/600
TF	9	0	0.33402	58	1200/2000

Table 5-3
RBWR-TB2 History Structure

History	Control Rod State	Core Average Moderator Density (g/cc)	Corresponding Void Fraction (%)	Fuel Temperature (K) (blanket/fissile)
1	0	0.33536	57	600/900
2	0	0.25929	68	600/900
3	0	0.50550	33	600/900
4	1	0.33536	57	600/900

Table 5-4
RBWR-TB2 Cross Section Branch Structure

Branches	Index	Control Rod State	Core Average Moderator Density (g/cc)	Corresponding Void Fraction (%)	Fuel Temperature (K) (blanket/fissile)
RE	1	0	0.33536	57	600/900
CR	2	1	0.33536	57	600/900
DC	3	0	0.00001	100	600/900
DC	4	0	0.25929	68	600/900
DC	5	0	0.50550	33	600/900
DC	6	0	0.76000	0	600/900
DC	7	1	0.76000	0	600/900
TF	8	0	0.33536	57	500/600
TF	9	0	0.33536	57	1200/2000

The SerpentXS script developed at MIT was used to execute the Serpent code for all of the branching and history calculations [7]. Each state condition is specified within the SerpentXS input and the code generates Serpent input files for all of the history and branch cases. Once the inputs are generated, SerpentXS submits each calculation for simulation. This process can involve hundreds or even thousands of Monte Carlo simulations to model each of the specified branches for each burnup step of interest. For the purposes of this analysis, it was necessary to perform a total of 880 simulations for 22 burnup points with 10 branches and 4 histories. Only 9 of the 10 branches generated were used in the PARCS simulations because PARCS often had trouble converging when the high void, control rod inserted cross branch was included.

Generating cross sections for the radial reflector required an unusual approach in Serpent. Typical methods for generating radial reflector cross sections involve generating a 2D fuel-reflector interface with reflective boundary conditions on all sides except for the reflector-boundary interface which is set as a vacuum boundary. The fuel and reflector lengths are set such that they cover several mean free paths. However, Serpent requires that the same boundary condition must be applied for all surfaces in a set Cartesian direction (for example, the left and right boundaries of a problem must have the same boundary condition).⁴ Three separate boundary conditions can be applied in the x, y, and z direction. To avoid any issues with the boundary conditions, 2D fuel-reflector interface problems were created such that the typical reflective boundary condition applied on the fuel-boundary interface was modified. Instead of using a reflective boundary condition, a mirror image of the model was placed next to the existing model such that there is a single large lattice of fuel elements in the center surrounded by a reflector model on either side. This leads to a geometry that is twice the size of a typical radial reflector cross section calculation, but avoids the issue of not being able to apply separate boundary conditions in the same direction. The model can be seen in Fig. 3-5.

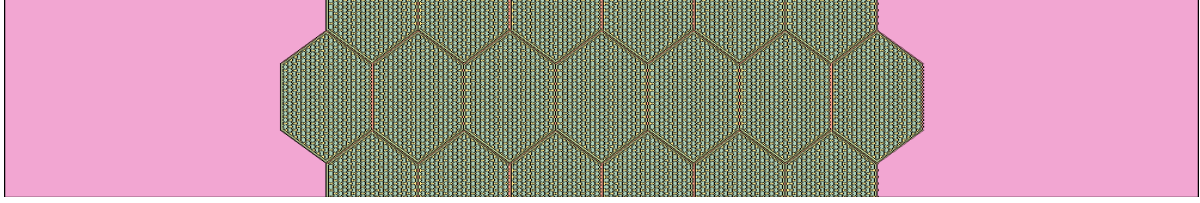


Figure 3-5. Supercell for modeling radial reflector cross sections.

A separate 2D fuel-reflector interface problem was created for each of the fuel regions (5 for the AC, 4 for the TB-2) to capture the spectral effects in the different regions. An average of the coolant density within each region was used for the coolant density inside the fuel elements. Inside the reflector, the saturation density of the coolant was used. All of the Monte Carlo calculations were done with the control rods removed from the fuel elements.

3.2b Cross Section Processing

Serpent simulations with user specified tallies produce a significant amount of data for the generation of the group constants. However, this data must be tabulated and organized for use with a nodal diffusion code such as PARCS. The GenPMAXS code [8] was developed to convert lattice level output into a usable format (PMAXS) for the core simulator PARCS. Prior to the creation of Serpent, the code supported multiple lattice codes including HELIOS, CASMO, WIMS, CONDOR and TRITON. Additional coding was introduced into the GenPMAXS code which now supports both Serpent and Serpent2. The GenPMAXS code is also capable of performing several other group constant calculations that are not supported within Serpent, including the calculation of axial discontinuity factors.

The use of 3D cross sections for the RBWR was first investigated at MIT in 2011 [7]. During that study, it was found that 3D cross sections alone were not sufficient in reproducing a similar 3D Monte Carlo solution. This led to the creation of axial discontinuity factors (ZDF) which are similar to the conventional assembly discontinuity factors (ADF)⁸ except for the axial direction. For a given axial interface, a ZDF is defined as the ratio of the heterogeneous surface flux to the homogeneous surface flux:

$$f = \frac{\phi_{s,i,g}^{het}}{\phi_{s,i,g}^{hom}} \quad (1)$$

Where the heterogeneous surface flux is approximated using the partial currents from Serpent:

$$\phi_{s,i,g}^{het} = 2(J_{i,g}^{+} + J_{i,g}^{-}) \quad (2)$$

And the homogeneous surface flux is found by solving the one-dimensional axial diffusion equation using the nodal expansion method (NEM) for a single node with the calculated group constants. The homogeneous surface flux is solved using the same method as PARCS (NEM for

this case) in order to reproduce the Monte Carlo solution. The NEM approximates the flux solution within each mesh region using a fourth order Legendre polynomial:

$$\bar{\phi}(\xi) = \sum_{i=0}^4 \bar{a}_i P_i(\xi) \quad (3)$$

The five coefficients associated with the flux expansion derive from the heterogeneous cell average flux, the net currents on the top and bottom surfaces and two weighted residual equations. The homogeneous surface fluxes for the top and bottom surfaces are found using the evaluated coefficients:

$$\bar{a}_0 = \bar{\phi} \quad (4)$$

$$\left(\bar{A} + \frac{5\bar{D}}{2h^2} \right) \bar{a}_1 = -\frac{5}{4h} (\bar{J}^B + \bar{J}^T) \quad (5)$$

$$\left(\bar{A} + \frac{21\bar{D}}{2h^2} \right) \bar{a}_2 = -\frac{7}{4h} (\bar{J}^B - \bar{J}^T) \quad (6)$$

$$\bar{a}_3 = -\frac{h}{12\bar{D}} (\bar{J}^B + \bar{J}^T) - \frac{1}{6} \bar{a}_1 \quad (7)$$

$$\bar{a}_4 = \frac{h}{20\bar{D}} (\bar{J}^B - \bar{J}^T) - \frac{3}{10} \bar{a}_2 \quad (8)$$

$$\bar{\phi}_{i,g}^{B,Hom} = \bar{a}_0 - \bar{a}_1 + \bar{a}_2 - \bar{a}_3 + \bar{a}_4 \quad (9)$$

$$\bar{\phi}_{i,g}^{T,Hom} = \bar{a}_0 + \bar{a}_1 + \bar{a}_2 + \bar{a}_3 + \bar{a}_4 \quad (10)$$

The axial discontinuity factors are included in the PMAXS cross section file for the top and bottom surfaces of a given material node. A separate cross section file was created for each nodal region to accommodate the axial discontinuity factors and the 3D cross sections.

For interfaces with large gradients, such as the region between seed and blanket zones, the homogeneous flux can become negative which leads to a negative discontinuity factor. This can result in negative fluxes within PARCS and numerical problems during the flux solution. A scheme was developed to avoid this based on modifying the diffusion coefficient such that the axial discontinuity factor would be bounded within an acceptable range, while still preserving the net current on the node interface. However, the modification of the diffusion coefficient also affected the radial 2D calculation within TPEN causing instabilities within the core calculation. Instead, limits were placed on the axial discontinuity factors. If the calculated value exceeded the specified range, then the quantity was changed to the closest bound.

3.2c Full Core Modeling

The final stage of the core simulator consists of executing the coupled codes PARCS [10] and PATHS [12]. For the tight pitch lattice in the RBWR, the hexagonal nodal diffusion kernel is used in PARCS which is based on the triangular polynomial expansion method (TPEN) to solve for the few group fluxes in the radial direction. As noted earlier, the axial flux is solved using the 1D NEM method and coupled to the radial solution using the traditional transverse leakage

approximation. The codes are coupled with PARCS providing the node-wise powers to PATHS, while PATHS provides PARCS with the fuel temperature, coolant density and coolant temperature. The two codes iterate until a converged solution is achieved.

The principle application of this coupled code simulator in the work here is to calculate the equilibrium cycle of the RBWR. This is an iterative process that consists of depleting the full core and then shuffling the fuel bundles. The process is repeated until a desired maximum burnup difference between fuel recycles is met. For the RBWR, a convergence criterion of 0.1 GWd/t on the infinite norm of the node-wise burnup matrix at EOEC was used. Depletion was performed using the control rod movement and fuel shuffling pattern specified by Hitachi [16,17].

3.3a PARCS Modeling

PARCS [10] (Purdue Advanced Reactor Core Simulator) is a three dimensional reactor core simulator which solves steady-state and time-dependent, multi-group neutron diffusion and SP3 transport equations in cartesian, cylindrical, and hexagonal geometries. PARCS is coupled directly to the thermal-hydraulics code PATHS (for equilibrium cycle simulation) and TRACE (for transient simulation), which provide the temperature and flow field information to PARCS. The major calculation features in PARCS include the ability to perform eigenvalue calculations, transient (kinetics) calculations, Xenon transient calculations, decay heat calculations, pin-power calculations, and adjoint calculations for commercial Light Water Reactors. The hexagonal nodal method was used to model the RBWR core and has been previously tested for fast reactor applications using multigroup hexagonal nodal solutions [11].

The RBWR core consists of 720 fuel assemblies (FA), is 1/3 rotationally symmetric, and the rated core power is 3926 MWth [2]. A ring of hexagonal nodes whose total area is equal to 34 times the area of a single FA is used to represent the radial reflector region. The PARCS model represents separately each of the 240 FAs (1/3 of 720 FAs in total). The active core height is 134.4 cm for the RBWR-AC core which is modeled in PARCS with the same 36 layers of axial discretization as done in Serpent. The thickness of the axial layers is 0.875 cm, 3.5 cm, 6.5 cm, 2.4125 cm and 5.6 cm for upper blanket, upper fissile zone, internal blanket, lower fissile zone, and lower blanket, respectively. A single mesh per fuel assembly is used in the radial plane, which was deemed sufficient based on a sensitivity analysis. At the top of the active core, there exists a 30 cm-thick axial reflector region; the upper boron layer of the top reflector is replaced by a vacuum boundary condition. The bottom reflector is 30 cm thick. The bottom 23 cm is just water and the top 7 cm contain B₄C pins. Only the top 7 cm are modeled in PARCS. Below the reflector is simply a vacuum boundary condition. Only the upper 7 cm of the lower reflector are modeled explicitly in PARCS. It should be noted there are limitations in the representation of both the top and bottom reflectors that could be improved with full core 3D Monte Carlo methods. However, the approximations in the existing models were deemed acceptable for purposes of the equilibrium cycle search and transient model, which are the principle objectives of the core simulator.

The RBWR-AC axial configuration of the core geometry for the PARCS model is given in Table 3-5.

Table 3-5
Axial configurations of the RBWR-AC core geometry for PARCS model

Zone	Number of Mesh	Total Length (cm)
Upper Reflector	1	30
Upper Blanket Region	5	7
Upper Fissile Region	8	28
Internal Blanket	8	52
Lower Fissile Region	8	19.3
Lower Blanket Region	5	28
Lower Reflector	1	7

The RBWR-TB2 has a core height of 102.1 cm and utilizes one less blanket region (there is no lower blanket region). The 2.0 cm upper blanket region was modeled as two 1.0 cm regions in both the neutronic and thermal hydraulic meshes. The axial meshing was changed from Hitachi's (ten 0.2 cm planes) because the 1D NEM in PARCS cannot converge with such exceedingly thin regions as those used in the upper blanket region of Hitachi's model. Hitachi likely uses a finite difference method in the axial direction, which can converge to a solution even for these very thin planes. The thickness of the axial layers is 5.425 cm, 7 cm and 5.6 cm for upper fissile, internal blanket, and lower fissile, respectively. At the top and bottom of the active core, there are 30 cm-thick axial reflector regions. Unlike the AC, the lower reflector for the TB2 model does not contain boron. It is just a 30 cm water region, so the whole reflector region was modeled explicitly in PARCS. Vacuum boundaries were applied at the top and bottom of the reflectors. The axial configuration of the core geometry for the RBWR-TB2 PARCS model is shown in Table 3-6.

Table 3-6
Axial configurations of the RBWR-TB2 core geometry for PARCS model

Zone	Number of Mesh	Total Length (cm)
Upper Reflector	1	30
Upper Blanket	2	2
Upper Fissile Region	8	21.7
Internal Blanket	8	56
Lower Fissile Region	8	22.4
Lower Reflector	1	30

3.3b PATHS Modeling

PATHS [12] (PARCS Advanced Thermal Hydraulic Solver) has been developed to calculate a steady-state thermal-hydraulics solution for LWRs. PATHS is simpler than six-equation, two-fluid codes such as TRACE or RELAP5, which have a higher fidelity than is necessary to perform steady-state coupled neutronics/thermal-hydraulics calculations for deple

tion analysis. Because of this, PATHS runs more quickly and allows for improved turnaround time during core analysis. The efficiency of PATHS makes one-to-one neutronics/thermal-hydraulics coupled calculations practical, even for very quick and simple calculations.

PATHS utilizes a four-equation drift flux model with simplified equations and solution algorithms which considerably reduce the runtime. User-specified boundary conditions include outlet pressure, total core mass flow rate, and inlet enthalpy. The following description is from the PATHS manual [12].

“The PATHS methodology is based on the two fluid model developed by Ishii [13], averaged to consider the mixture instead of two separate fluids. The finite volume method is applied and the equations are cast into a face-based scheme. Since the control volume is set to include the entire cross-sectional area in a channel, the equations are reduced to a one-dimensional flow with heat fluxes and stress terms coming from the boundary. The void fraction and drift velocity are introduced through constitutive relationships instead of a fourth field equation that would normally show up in the drift flux model.”

The discretized conservation equations for mass, momentum, and energy, are given by

$$(\rho_m^* v_m A)_n - (\rho_m^* v_m A)_s = 0 \quad (12)$$

$$\left(\rho_m^* |v_m^*| v_m \left(A + \frac{1}{2} F_z^* \Delta V \right) \right)_n - \left(\rho_m^* |v_m^*| v_m \left(A - \frac{1}{2} F_z^* \Delta V \right) \right)_s + (PA)_n - (PA)_s \quad (13)$$

$$= \left(\frac{\alpha^*}{1 - \alpha^*} \frac{\rho_f^* \rho_g^*}{\rho_m^*} v_{gj}^{2*} A \right)_s - \left(\frac{\alpha^*}{1 - \alpha^*} \frac{\rho_f^* \rho_g^*}{\rho_m^*} v_{gj}^{2*} A \right)_n - \frac{(\rho_m^*)_n + (\rho_m^*)_s}{2} g \Delta V$$

$$F_z^* = \frac{1}{2} \left(\frac{\Phi_{2\Phi} f}{D_h} + \frac{K_{loss}}{\Delta z} \right) \quad (14)$$

$$((\rho_m^* v_m^* h A)_n) - ((\rho_m^* v_m^* h A)_s) = q_{wall}'' \xi_h \Delta z + \left(\alpha^* \frac{\rho_f^* \rho_g^*}{\rho_m^*} \Delta h_{fg}^* v_{gj}^* A \right)_s - \left(\alpha^* \frac{\rho_f^* \rho_g^*}{\rho_m^*} \Delta h_{fg}^* v_{gj}^* A \right)_n$$

$$+ \left(v_m^* + \frac{\alpha^* (\rho_f^* - \rho_g^*)}{\rho_m^*} \bar{v}_{gj} \right) ((P^* A)_n - (P^* A)_s) \quad (15)$$

where standard greek letters are used to refer fluid quantities (e.g. ρ for density) and the subscripts f, g , and m denote fluid (liquid), gas, and mixture, respectively.

The user may choose from various void correlations. The void correlations in PATHS are appropriate for standard BWRs. The default is an EPRI void model, which is sufficient for the RBWR-TB2 because of the lower fuel-to-moderator ratio. However, because of the tight-pitch fuel design of the RBWR-AC, the EPRI correlation produces a poor model of the physical void distribution. The available experimental data for tight-pitch BWR assemblies was compared

against several different void correlations to get a more accurate model [14]. The Lia, Parlos, and Griffith (LPG) model was determined to most closely match experimental data, and was subsequently implemented in PATHS and TRACE and used for all equilibrium cycle and transient analysis of the RBWR-AC. It should be noted that Hitachi has a different void correlation which was used for both the AC and TB2 models. In general, this model predicts a higher void fraction than LPG and shows similar results to the EPRI correlation. Fig. 3-6 shows the effect of the void correlation on a single-channel PARCS-PATHS simulation.

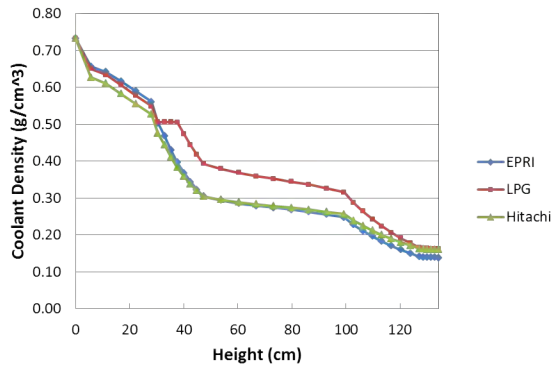


Figure 3-6a: RBWR-AC Void Correlation Comparison (LPG used)

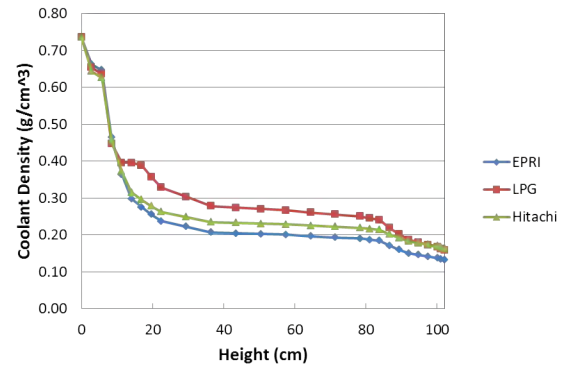


Figure 3-6b: RBWR-TB2 Void Correlation Comparison (EPRI used)

3.3c Shuffling Pattern/Control Rod Sequence

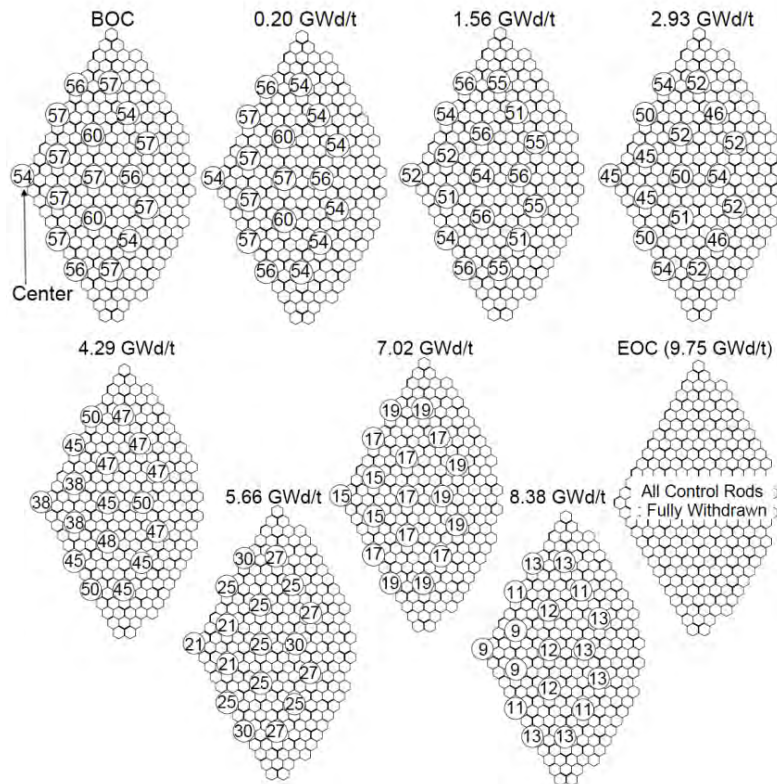


Figure 3-7. RBWR-AC Control Rod Pattern

An iterative algorithm has been developed to provide nested iterations to determine the equilibrium core configuration using the SERPENT/PARCS/PATHS code system. It takes into consideration explicit treatment of fuel bundles shuffling and control rod scheduling as defined in Hitachi supplement documents and the core was depleted with PARCS by steps defined by the specified control rod sequence shown in Fig. 3-7. The control rod sequence pattern provided by Hitachi, which divides one fuel cycle into nine stages, is used for core reactivity control during the cycle. The fuel Shuffling Pattern provided by Hitachi (Fig. 3-8) is used for multi-cycle fuel loading.

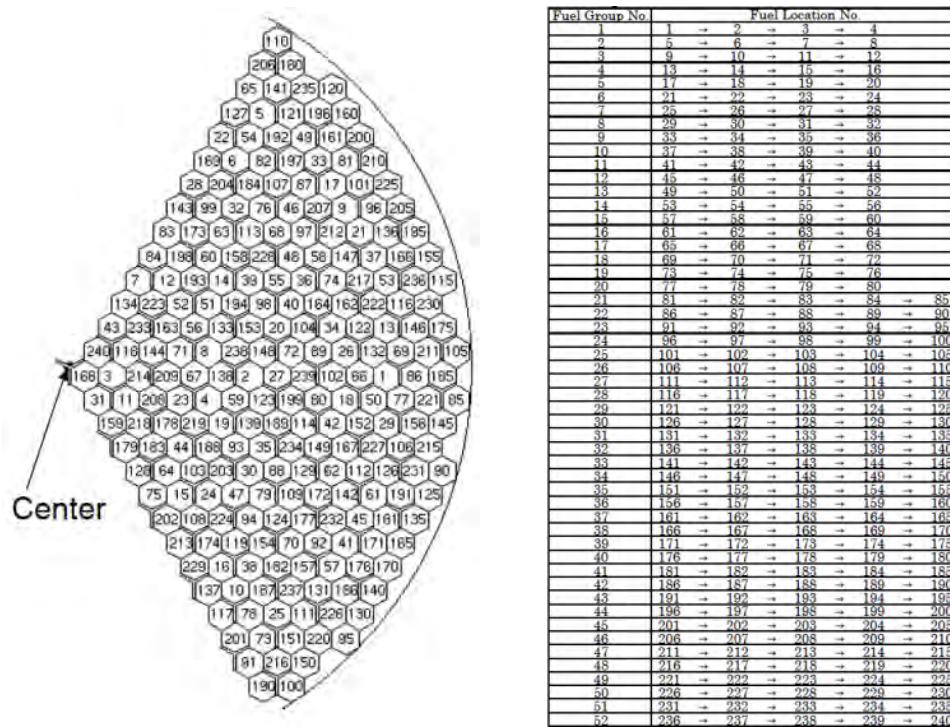


Figure 3-8. RBWR-AC Shuffling Pattern

The equilibrium cycle calculation was performed using the design parameters produced by Hitachi for both the AC and TB2 shown in Tables 3-7 and 3-8, respectively [16,17]. Many of the important parameters are identical, including thermal power rating, number of fuel bundles, maximum linear heat generation rate (MLHGR), and minimum critical power ratio (MCPR). The main difference is in the fuel geometry and composition. The greater number of pins in the TB2 counteract the shorter active core height to keep the MLHGR from increasing. The TB2 is loaded with approximately half as much heavy metal as the AC, but the fuel has a higher fissile plutonium enrichment. The coolant flow rate is slightly higher in the AC, but both designs call for a varied flow rate throughout the cycle.

3.3d Equilibrium Cycle Search Methodology

An equilibrium cycle search algorithm was implemented for the coupled codes. The convergence criterion was set to 0.1 GWD/T for the infinite norm of node-wise burnup at the End of Cycle (EOC). The overall flowchart is shown in Fig. 3-9.

Table 3-7
Hitachi Design Parameters for the
RBWR-AC

Item		RBWR-AC
Thermal Power	MWt	3926
Electrical Power	MWe	1356
No. of Fuel Bundles		720
Core Height	mm	1343
Configuration for Height		Parfait
Coolant Flow Rate	kt/h	26
Core Exit Quality	%	35
Void Fraction	%	53
Pressure Drop	MPa	0.14 *
HM Inventory	t	144
Puf/HM in Fissile Zone w/o		15.7 / 20.1
Puf Inventory	t	9.0
Burnup	GWd/t	45
MLHGR	kW/ft	14.4
MCPR		1.28
Void Coef.	$\Delta k/k/\% \text{void}$	-2.4×10^{-4}
Breeding Ratio		1.01

* active core region

Table 3-8
Hitachi Design Parameters for the
RBWR-TB2

Item		RBWR-TB2
Thermal Power	MWt	3926
Electrical Power	MWe	1356
No. of Fuel Bundles		720
Core Height	mm	1021
Configuration for Height		Parfait
Coolant Flow Rate	kt/h	24
Core Exit Quality	%	36
Void Fraction	%	56
Pressure Drop	MPa	0.06 *
HM Inventory	t	75.4
Puf/HM in Fissile Zone w/o		24.9
Puf Inventory	t	8.2
Burnup	GWd/t	65
MLHGR	kW/ft	14.4
MCPR		1.28
Void Coef.	$\Delta k/k/\% \text{void}$	-4×10^{-4}
TRU Fission Efficiency %		45

* active core region

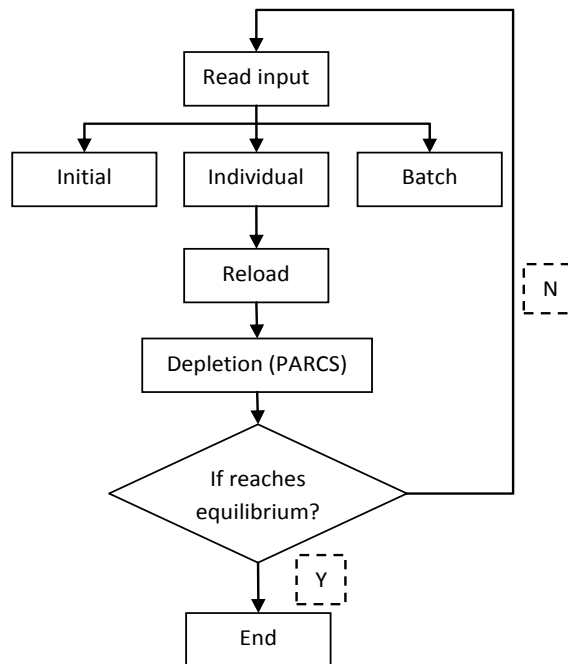


Figure 3-7. Equilibrium Cycle Search Flowchart

Chapter 4: PARCS-PATHS Analysis

The RBWR results are discussed in two sections: a single assembly analysis and full core analysis. For the first section, the ability to reproduce the Monte Carlo solution using 3D Serpent cross sections in PARCS is demonstrated for the single assembly. The second part extends the calculation to full core simulations for equilibrium cycle analysis.

4.1 Single Assembly Analysis

In order to demonstrate that 3D cross sections with axial discontinuity factors can reproduce the reference Monte Carlo solution, a single assembly benchmark problem was simulated. The Serpent calculation was performed using 150,000 source particles per cycle with 300 active cycles and 100 inactive cycles using ENDF/B-VII neutron cross section library. Reflective boundary conditions were applied to all sides of the assembly and group constants were found for each axial level. Based on previous experience, axial discontinuity factors were bounded over the range of 0.85 to 1.15 to mitigate potential numerical issues in PARCS. Cross sections were collapsed to 12 energy groups based on previous Hitachi studies [1]. The same model was generated in PARCS and the cross sections from Serpent were used in the PARCS simulation. Table 4-1 shows the comparison of the single assembly results.

Table 4-1
Eigenvalue Comparison for Single Assembly Case

Method	k	Difference from Serpent (pcm)
3D Serpent	1.09601	-
3D PARCS without ZDFs	1.08772	-829
3D PARCS with ZDFs – no D treatment	1.09645	44
3D PARCS with ZDFs – D treatment	1.09601	0

When using only 3D cross sections, with a relative error of 9.6 pcm on k-eff for the Monte Carlo solution, the PARCS solution is over 800 pcm different from the Monte Carlo solution. When axial discontinuity factors are introduced without any modification of the diffusion coefficient (if a discontinuity factor lies outside of the specified bounds, it is set to the closest bound), there is a small difference of 44 pcm. Finally, if 3D cross sections with axial discontinuity factors and diffusion coefficient treatment are used, PARCS reproduces the exact Monte Carlo solution.

A comparison of the normalized fluxes between Serpent and PARCS for an RBWR-like assembly with and without axial -discontinuity factors for the fast (group 1) and thermal (group 9) are shown in Fig. 4-1. These plots represent the flux over the active core region. From 0-30 cm represents the lower blanket, 30-50 cm the lower fissile, 50-100 cm the internal blanket, 100-130 cm the upper fissile and 130-140 cm the upper blanket. Each of these regions is divided by a solid line in the Figure. For the fast group, the PARCS solution without axial discontinuity factors underestimates the flux in the lower fissile zone and over predicts the flux in the blanket regions near the upper fissile zone. With axial discontinuity factors, the solution is consistent with the Serpent flux profile. For the thermal group, the PARCS solution without axial discontinuity factors underestimates the flux in the lower fissile region. It also has difficulty

reproducing the solution in the upper blanket, where it over predicts the flux. The flux shape in the thermal group is not as smooth as the fast group flux shape and it is much more difficult for the diffusion solution to reproduce the Monte Carlo solution without the use of axial discontinuity factors. The flux comparisons for all 12 energy groups can be found in Appendix A.

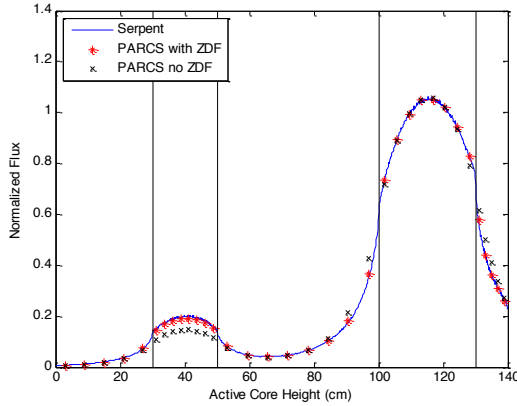


Fig. 4-1a. Fast (group 1) flux comparison.

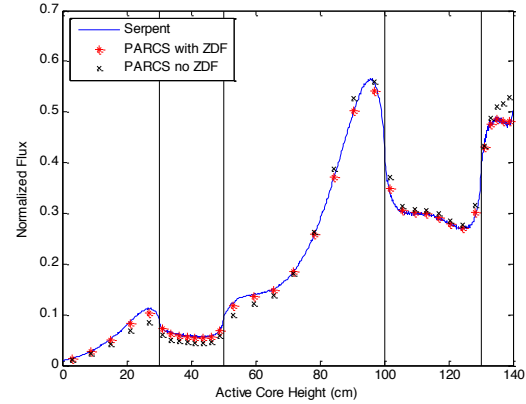


Fig. 4-1b. Thermal (group 9) flux comparison.

For the equilibrium cycle analysis, the method was modified in order to achieve stability and accuracy of the solution. While modifying the diffusion coefficient allows the deterministic solution to match the Monte Carlo solution exactly for a single assembly (Table 4-1), the modified diffusion coefficients were adversely affecting the radial streaming in the core simulation. Thus, modifying the diffusion coefficient to keep the ZDFs within a reasonable range was unfeasible. Instead, the ZDFs were simply bounded (between 0.85 and 1.15) without significant detriment to the accuracy of the solution. Any ZDF outside of this range was simply set to the nearest bound.

4.2 Equilibrium Cycle Analysis - AC

The discussed methods were applied to full core analysis and the calculation of an equilibrium cycle. 3D cross sections were generated for the history and branching scheme discussed in the previous sections. Bounded axial discontinuity factors were created for all nodes and appended to the PMAXS files. A one-third core PARCS model of 240 assemblies was used with a one-to-one channel mapping to the thermal-hydraulics code PATHS.

Node-wise burnups were extracted from Serpent for each homogenized region and PMAXS cross sections were generated for all 39 axial regions. The simulation required 11 iterations (fuel shuffles) to converge as shown in Fig. 4-2. There are 52 new assemblies loaded into the core each cycle, or 21.7% of the 240 modeled. 32 assemblies are burned five times, while the other 20 are removed after the fourth cycle.

The burnup swing over the equilibrium cycle is 9.75 GWd/t with a maximum discharge burnup of 116.7 GWd/t in the fuel. The eigenvalue is subcritical, with a swing from 0.987755 at

beginning of equilibrium cycle (BOEC) to 0.984859 at end of equilibrium cycle (EOEC). Comparisons of the axial power profile to previous Hitachi data (Fig. 4-3) [16] shows that the results see a constant peaking in the lower fissile region and a smaller relative power contribution in the upper blanket region. Additionally, unlike the PARCS simulations, the Hitachi data was derived from traditional 2D cross section sets using JENDL-3.2 nuclear data libraries. The radial power distribution shown in Fig. 4-4 is similar to the trend reported by Hitachi [16]. Differences in the results are likely due to the library treatment and generation of cross sections. A recent collaboration with Hitachi assessed the impact of the different libraries using the 3D Monte Carlo codes MVP and SERPENT [15]. Several depletion points were analyzed and can be seen below in Table 4-2. The use of the ENDF/B-VII nuclear data library instead of JENDL-3.2 results in a 1% increase in eigenvalue and good agreement between the MVP and SERPENT codes. Differences at higher burnup are attributed to the decay chain data used in both simulations. By altering the nuclear data and analyzing the RBWR assembly using 3D Monte Carlo, the results between Michigan and Hitachi are now converging. Future collaboration with Hitachi is planned to resolve any remaining differences.

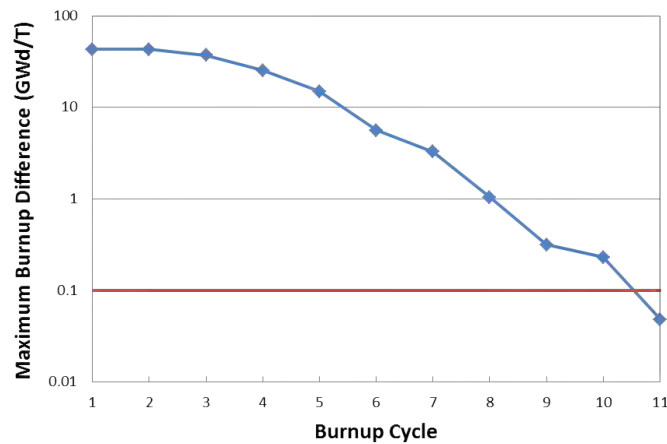


Figure 4-2. RBWR-AC Equilibrium cycle convergence.

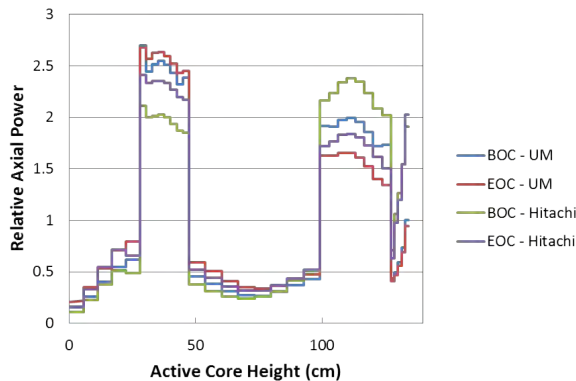


Figure 4-3. RBWR-AC Relative axial power distribution.

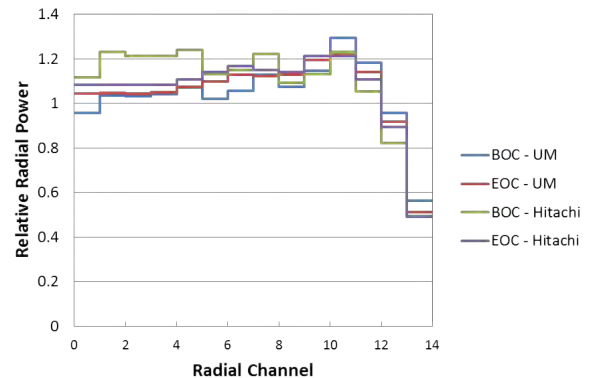


Figure 4-4. RBWR-AC Relative radial power distribution.

Table 4-2
Serpent-MVP Depletion Comparison

				difference(pcm)	
GWd/t	SERPENT (ENDF7)	MVP(J32)	MVP (ENDF7)	MVP(J32)- SERPENT	MVP(ENDF7)- SERPENT
0	1.060100	1.049760	1.059600	-929	-45
0.25	1.059210	1.048550	1.058510	-960	-62
0.5	1.060960	1.050410	1.060120	-947	-75
1	1.063530	1.052720	1.062080	-966	-128
2	1.065190	1.054410	1.063690	-960	-132
4	1.063330	1.054270	1.062550	-808	-69
6	1.060370	1.051570	1.059590	-789	-69
8	1.055710	1.047990	1.055380	-698	-30
10	1.050730	1.044600	1.051290	-558	51
15	1.038540	1.034670	1.039820	-360	119
20	1.027140	1.024750	1.029000	-227	176
25	1.016660	1.014940	1.018720	-167	199
30	1.006080	1.005640	1.008250	-43	214
35	0.996061	0.996411	0.998769	35	272
40	0.986520	0.987726	0.989544	124	310
45	0.977514	0.979669	0.980790	225	342
50	0.969207	0.971934	0.972306	289	329
70	0.938998	0.944111	0.943386	577	495
90	0.914564	0.921232	0.919582	791	597
110	0.894807	0.902634	0.900788	969	742
130	0.877344	0.886583	0.884936	1188	978

4.3 RBWR-AC Reactivity Coefficients

Several core states were calculated using PATHS/PARCS to determine the reactivity coefficients. Cases were set up at $\pm 10\%$ of nominal power and $\pm 10\%$ of nominal flow rate. All cases were based on the equilibrium cycle results reported above.

For the flow perturbation cases, the inlet velocity was changed in PATHS. PATHS and PARCS were run iteratively to generate a consistent axial power and coolant density distributions. The calculated eigenvalue and void distribution were used together with the corresponding reference case results to calculate the void coefficient of reactivity.

For the power perturbation case, the Doppler coefficient was calculated by also determining the average fuel temperature for the reference and perturbed cases. Because the change in power and flow rate induce changes in the reactivity from both the Doppler and Void effects, the reactivity change from a single perturbed case cannot be used to calculate a partial derivative reactivity coefficient directly.

Therefore, the following linear system of equations was used to solve for the void and Doppler partial derivatives simultaneously using the output from two PARCS perturbed cases:

$$\begin{bmatrix} \Delta Void1 & \Delta Temp1 \\ \Delta Void2 & \Delta Temp2 \end{bmatrix} \begin{bmatrix} C_Void \\ C_Temp \end{bmatrix} = \begin{bmatrix} \rho1 \\ \rho2 \end{bmatrix}$$

Where $\Delta Void1$ is the change in average void fraction for the 90% or 110% flow cases and $\Delta Void2$ is the change in average void fraction for the 90% or 110% power cases. $\Delta Temp1$ is the average fuel temperature for the 90% or 110% flow cases and $\Delta Temp2$ is the change in average fuel temperature for the 90% or 110% power cases. The variable $\rho1$ is the change in reactivity associated with the 90% or 110% flow cases, and $\rho2$ is the change in reactivity associated with the 90% or 110% power cases. C_Void and C_Temp are the void and Doppler coefficients respectively.

The void coefficients calculated with PARCS-PATHS (Table 4-3) are slightly smaller in magnitude than those reported by Hitachi (Table 4-4), but still negative. This result is logical because UM predicts a lower power contribution by the upper blanket. The predicted swing over the depletion cycle is similar in magnitude. The void coefficient is not monotonically decreasing in magnitude throughout the cycle (Fig. 4-5). There are two main competing effects that cause the void coefficient to change. As the fuel is burned, Pu-239 is bred from U-238, which makes the void coefficient less negative. However, the void coefficient is strongly dependent on the spectrum, which is affected by the moderator density (void distribution). The void distribution changes significantly throughout the cycle due to a coolant mass flow rate that varies from as low as 5600 kg/s in the middle of the cycle to 7130 kg/s at the end, and also a shift in power towards the bottom of the core later in the cycle. Because the amount of fissile plutonium is greatest at the end of the equilibrium cycle, the void coefficient of reactivity is least negative at this point. The magnitude of the coefficient peaks near the beginning of the cycle at around -32 pcm/% void. It is useful to know the peak value because a void coefficient that is very strongly negative can cause instabilities.

Table 4-3
RBWR-AC Reactivity Coefficients (UM)

	Doppler (pcm/K)		Void (pcm/%Void)	
	90% Power	110% Power	90% Flow	110% Flow
BOC	-2.8	-2.8	-32	-30
EOC	-3.0	-2.9	-12	-10

Table 4-4
RBWR-AC Reactivity Coefficients (Hitachi)

	Doppler (pcm/K)		Void (pcm/%Void)	
	90% Power	110% Power	95% Flow	105% Flow
BOC	-2.4	-2.3	-34	-32
EOC	-2.4	-2.4	-24	-22

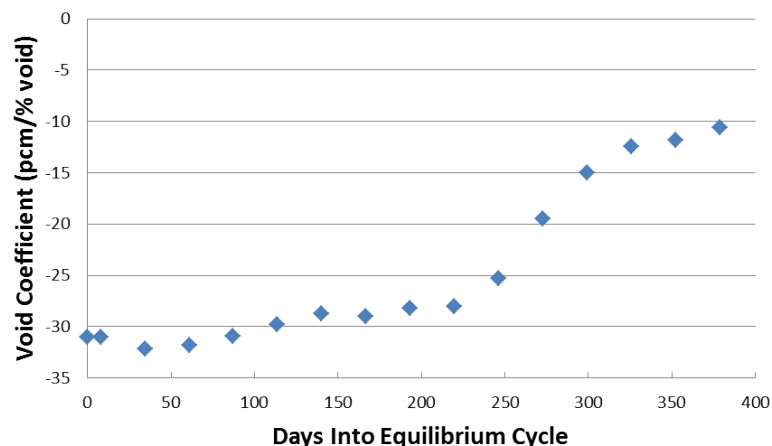


Figure 4-5. Effect of Depletion on Void Coefficient of Reactivity, RBWR-AC

The TRU composition of fuel at the end of life is given in Table 4-5. The compositions are mostly in good agreement, except for Am-241, Pu-240, and Pu-241. This is likely due to a difference in the decay chains within Serpent and MVP (Hitachi lattice code) and their treatment of Pu-241. The calculated fissile inventory ratio (FIR) was slightly greater than unity (1.01), which is in agreement with the Hitachi calculated value and verifies the self-sustaining capability of the AC reactor design.

**Table 4-5
RBWR-AC Discharge TRU Isotopic Composition**

	Hitachi	UM		Hitachi	UM
Np-237	0.47%	0.44%	Am-243	1.42%	1.33%
Pu-238	2.91%	2.90%	Cm-243	0.02%	0.02%
Pu-239	43.49%	43.50%	Cm-244	1.18%	1.07%
Pu-240	35.90%	36.32%	Cm-245	0.33%	0.34%
Pu-241	6.17%	5.12%	Cm-246	0.12%	0.10%
Pu-242	4.94%	5.05%	Cm-247	0.01%	0.02%
Am-241	2.82%	3.63%	Cm-248	0.02%	0.01%
Am-242m	0.19%	0.15%	FIR	1.01	1.01

4.4 Monte Carlo Void Coefficient Confirmation

Since the RBWR-AC has a smaller negative void coefficient than the RBWR-TB2, and the value calculated by UM is smaller in magnitude than what was calculated by Hitachi, there were still valid questions about how much confidence there is in the negative void coefficient. Because the spectrum (and its axial variation) is critical to getting the effective multiplication correct, a continuous-energy Monte Carlo model was used to calculate the void coefficient at the end of the equilibrium cycle. At this point in the cycle, the fissile plutonium inventory is the highest, and as a result the void coefficient is least negative. Therefore, this is a conservative case: if the void coefficient is negative at the end of the equilibrium cycle, it should be negative under all other normal operating conditions.

The Monte Carlo calculation was carried out by colleagues at Argonne National Laboratory (ANL). An RBWR model that was previously developed at MIT was updated with coolant density distributions calculated with the LPG void correlation. The Monte Carlo model had 15 axial zones and 5 radial regions (one for each batch). Each of the five axial fuel regions was divided into three separate axial zones. The material compositions were determined by a lumped-batch equilibrium cycle calculation with MCNP. For the nominal case, the coolant densities were extracted from the last step of the PARCS-PATHS equilibrium cycle. To get a perturbed coolant density distribution, PARCS-PATHS was restarted from the same step, but at 110% power. This resulted in a 2.66% increase in the core-average void fraction. MCNP was run with both coolant density distributions. The results are given in Table 4-6. The void coefficient is -17.3 (± 3.8) pcm/% void, which is not exceedingly different from what was calculated with PARCS-PATHS (-10 pcm/% void at EOC), considering that the fuel compositions were slightly different.

Table 4-6
Void coefficients at EOC for RBWR-AC using UM water densities (7160 kg/s)

EOC	keff	σ	Void Coefficient (pcm/%power)	σ (pcm/% power)	Void Coefficient (pcm/% void)	σ (pcm/% void)
nominal	0.98754	0.00007				
higher void	0.98708	0.00007	-4.7	1.0	-17.3	3.8

UM's water density distribution shown in Fig. 4-5 was calculated at the end of the cycle when the flow rate is ramped up as shown in Fig. 4-6, resulting in a softer spectrum which tends to yield a more negative void coefficient. Therefore, the water densities corresponding to a lower flow rate were also modeled to ensure that the void coefficient is negative at all points during the cycle. The minimum flow rate of 5600 kg/s occurs at around 7.7 GWd/t. The water densities corresponding to this statepoint are shown in Fig. 4-6, in light blue.

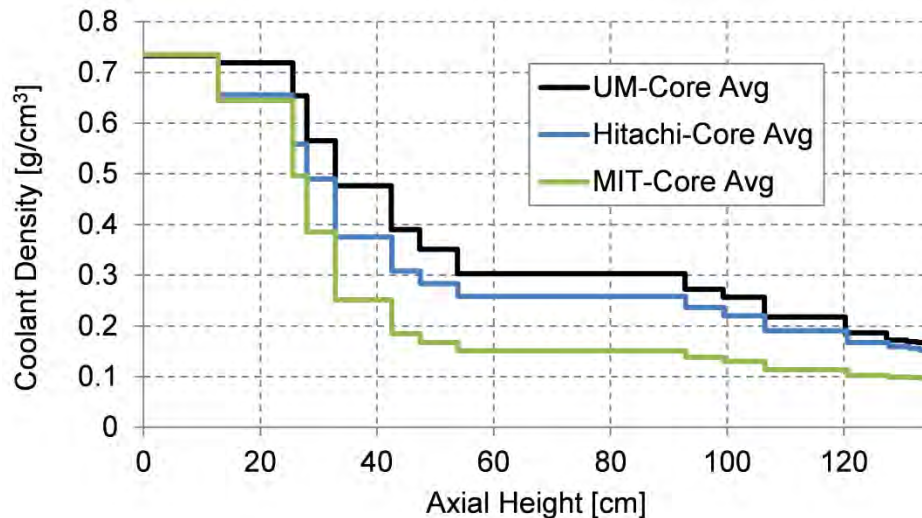


Figure 4-6. Core-average axial coolant density distributions

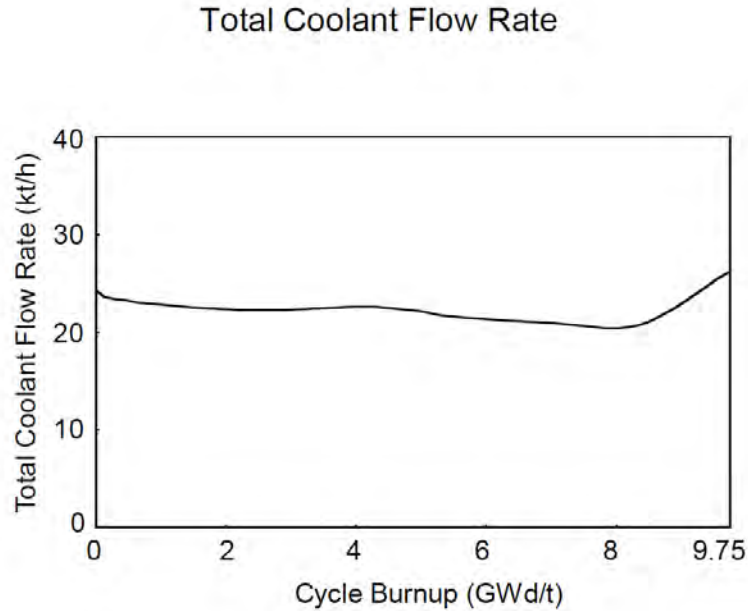


Figure 4-7. RBWR-AC coolant flow rate during equilibrium cycle

For conservatism (with respect to ensuring a nonpositive void coefficient), the fuel compositions at EOEC (9.75 GWd/t) were still used in the model, instead of the ones corresponding to the 5600 kg/s flow (at 7.7 GWd/t). The results in Table 4-7 show that this void distribution (Fig. 4-8) still resulted in a negative void coefficient beyond one standard deviation of numerical uncertainty (almost two standard deviations).

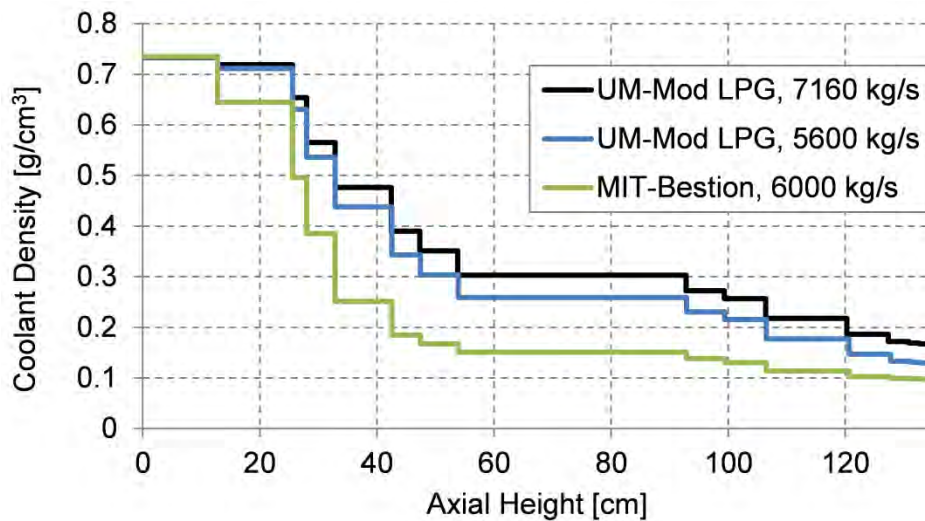


Figure 4-8. Core-average axial coolant density distributions with different flow rates

Table 4-7
Void coefficients at EOC for RBWR-AC using UM Densities (5600 kg/s)

EOC	keff	σ	Void Coefficient (pcm/%power)	σ (pcm/% power)	Void Coefficient (pcm/% void)	σ (pcm/% void)
nominal	0.98612	0.00007				
higher void	0.98594	0.00007	-1.9	1.0	-6.7	3.7

4.5 Equilibrium Cycle Analysis – TB2

The equilibrium cycle search for TB2 was performed with the same modifications to the core simulator. There are 60 fresh assemblies (out of 240) loaded into the core at the beginning of each cycle, and all assemblies are burned through four cycles. 10 cycles were required to converge the burnup distribution. Fig. 4-9 shows the convergence of the burnup distribution.

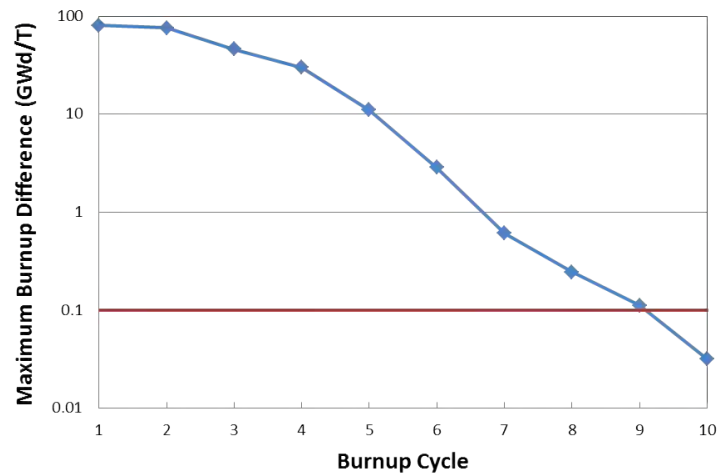


Figure 4-9. RBWR-TB2 Equilibrium cycle convergence.

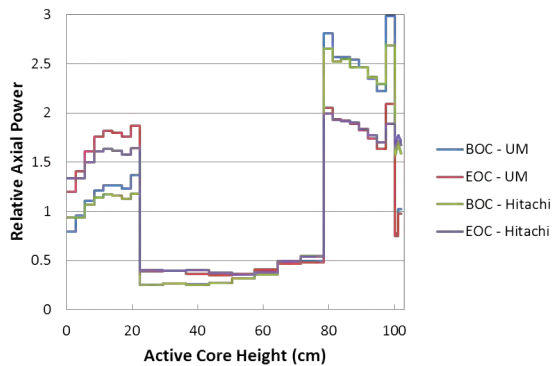


Figure 4-10. RBWR-TB2 Relative axial power distribution

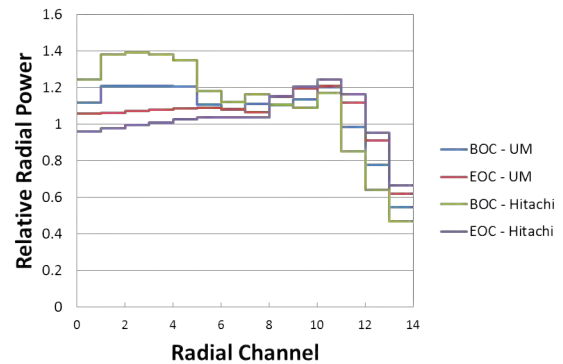


Figure 4-11. RBWR-TB2 Relative radial power distribution

The burnup swing over the equilibrium cycle is 16.25 GWd/t with a maximum burnup of 182.8 GWd/t in the fuel. The eigenvalue is subcritical, with a swing from 0.987678 at beginning of equilibrium cycle (BOEC) to 0.983974 at end of equilibrium cycle (EOEC). Comparisons of

the axial power profile to previous Hitachi data (Fig. 4-10) [17] shows that the results see a smaller relative power contribution in the upper blanket region. Fig. 4-10 also shows a higher peaking in the fissile fuel in zones adjacent to blanket regions. There is a large difference in the radial peaking factors (Fig. 4-11) which is likely attributable to differences in radial reflector modeling.

4.6 TB2 Reactivity Coefficients

The Doppler and void coefficients calculated with PARCS-PATHS (Table 4-8) are similar to those reported by Hitachi (Table 4-9). UM predicts a slightly larger swing in the magnitude of the void coefficient over the depletion cycle. Because there is, by design, less breeding of fissile plutonium in the TB2, the minimum calculated void coefficient is actually seen a few steps before the end of the cycle (Fig. 4-12). The void coefficient of reactivity is much more strongly negative for the TB2 than the AC. The peak value, which occurs slightly past the halfway point of the cycle, is -61 pcm/%void.

Table 4-8
RBWR-TB2 Reactivity Coefficients (UM)

	Doppler (pcm/K)		Void (pcm/%Void)	
	90% Power	110% Power	90% Flow	110% Flow
BOC	-1.6	-1.5	-53	-54
EOC	-2.0	-1.7	-37	-39

Table 4-9
RBWR-TB2 Reactivity Coefficients (Hitachi)

	Doppler (pcm/K)		Void (pcm/%Void)	
	90% Power	110% Power	95% Flow	105% Flow
BOC	-1.7	-1.7	-45	-44
EOC	-1.8	-1.7	-43	-43

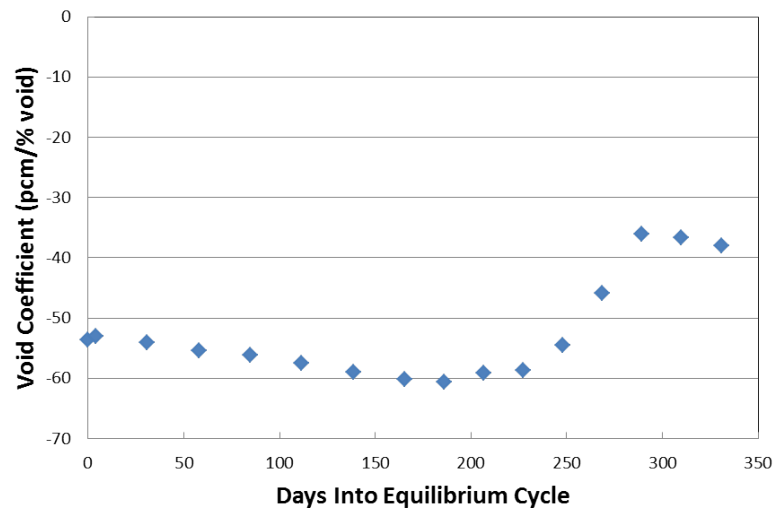


Figure 4-12. Effect of Depletion on Void Coefficient of Reactivity, RBWR-TB2

Table 4-10
RBWR-TB2 Discharge TRU Isotopic Composition

	Hitachi	UM		Hitachi	UM
Np-237	1.4%	1.4%	Am-241	1.4%	1.4%
Pu-238	6.6%	6.7%	Am-242m	4.6%	5.4%
Pu-239	25.5%	25.5%	Am-243	0.2%	0.2%
Pu-240	39.5%	40.1%	Cm-244	2.2%	2.0%
Pu-241	6.3%	5.4%	Cm-245	0.6%	0.6%
Pu-242	10.1%	10.1%	Cm-246	0.2%	0.2%

The TRU composition of fuel at the end of life is given in Table 17. The compositions are mostly in good agreement, except for Pu-241 and Am-242m. TRU fission efficiency is defined by Hitachi as the ratio the net reduction in TRU mass to the total amount of heavy metal fissioned throughout the life of the fuel (Eq. 16). UM predicts a fission efficiency of 44.3%, which is close to the value predicted by Hitachi, 45%.

$$\text{TRUs fission efficiency} = \frac{TRU_i - TRU_f}{HM_i - HM_f} \quad (16)$$

NOMENCLATURE

f = Axial discontinuity factor

$\phi_{s,i,g}^{het}$ = Heterogeneous surface flux

$\phi_{s,i,g}^{hom}$ = Homogeneous surface flux

$\bar{\phi}_{i,g}^{B,Hom}$ = Bottom homogeneous surface flux

$\bar{\phi}_{i,g}^{T,Hom}$ = Top homogeneous surface flux

$J_{i,g}^{+}$ = Positive partial current

$J_{i,g}^{-}$ = Negative partial current

\bar{J}^B = Bottom net surface current

\bar{J}^T = Top net surface current

$\bar{\phi}$ = Cell averaged flux

\bar{A} = Loss matrix

\bar{D} = Diffusion coefficient

h = Height of cell

i = Region

g = Energy group

FIR = ratio of fissile isotopes at end of cycle to beginning of cycle (fissile inventory ratio)

TRU = transuranic isotopes ($Z > 92$)

Chapter 5: Safety and Stability Modeling Development

For this study, the TRACE/PARCS v5785 code package was utilized as a starting point. The following models were implemented in the TRACE/PARCS code package and modeled using the updated package.

5.1a Critical Power Implementation

As supported by the documentation [18], the TRACE/PARCS code package has limited capability regarding critical power calculations. In order to perform the safety analysis of the RBWR-AC and RBWR-TB2 designs, these limitations had to be addressed. Therefore, the following improvements were made to the TRACE code's critical power calculation module:

- The internal module to calculate boiling length underestimated its value by a factor of 2. The modification to the code allowed satisfactory calculation of the boiling length which is only used for critical power and critical quality calculations.
- The internal code only calculated critical power for lengths larger than 1 m long. This limit was decreased to 0.5 m to encompass the shorter length of RBWR cores.
- Another parameter required for critical power calculations is the heated-to-wetted perimeter ratio. The code internally uses the inputted assembly width and the rod geometry assuming a square lattice configuration. Since the RBWR assemblies are hexagonal, the internal geometry calculation routine was modified to be able to correctly calculate the heated-to-wetted perimeter ratio.
- The internal code did not have any correlations applicable to RBWR type cores. Therefore, the MIT-CISE and HITACHI-CISE correlations [14] were implemented in the code replacing the BIASI critical quality correlation.

These implementations were verified by comparing to hand calculations on a single assembly basis.

5.1b Post Critical Power Heat Transfer Logic Implementation

According to the TRACE documentation [18], the role of critical quality in post CHF analysis is limited and requires additional modeling. The current method as shown by Fig. 5-1, primarily relies on the CHF temperature as the method to determine which post heat transfer regime will be assumed and for calculating the magnitude of the heat transfer correlation during the transition from inverted annular film boiling to dispersed flow film boiling. The CHF temperature is calculated from the 1995 AECL-IPPE CHF lookup tables. The application of local CHF values especially with very high peaking factors in the second fissile zone of the RBWR is very questionable. The mechanism of reaching boiling crisis has been experimentally

found by JAEA double humped experiments at RBWR type conditions to be dryout [19]. The inclusion of dryout instead of CHF temperature is not compatible with the interpolation post-CHF model for film boiling. Additionally, in case of core uncover toward the bottom of the core or during low power or pressure operating conditions, the local CHF consideration will be more appropriate than dryout.

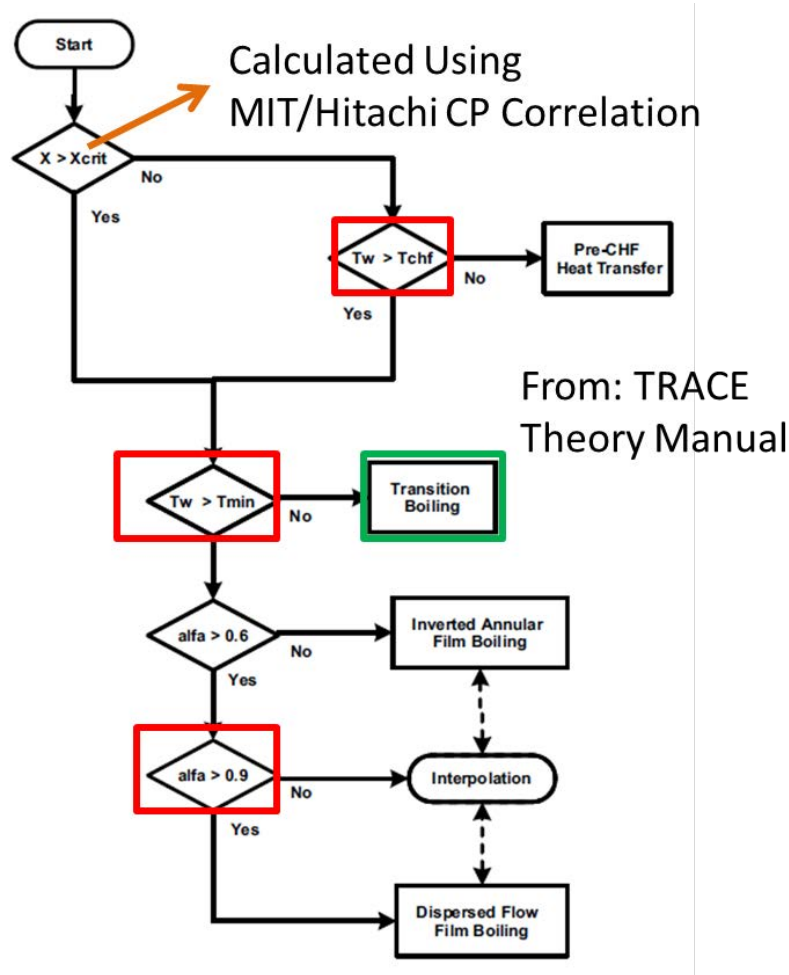


Figure 5-1. The post CHF wall heat transfer logic diagram implemented in TRACEv5 [18].

In order to calculate the minimum film boiling temperature for determination of post-CHF heat transfer, TRACE chooses the maximum temperature between quench temperature and film boiling temperature calculated by the Groeneveld-Steward model [18]. In TRACE, the quench temperature is assumed to be 725 K. The data shows the Groeneveld-Steward model is able to effectively capture the shape and magnitude of the quench temperature for pressures between 5-7 MPa, but for low pressures it underpredicts the quench temperature by ~100 K. The RBWR minimum film boiling temperature at operating conditions is ~650 K. For this work, the quench temperature is assumed to be 650 K to consistently model at ~7 MPa where the current safety analysis is restricted. Further considerations are required in order to accurately model the safety

performance of RBWR type reactors at low pressure (~ 2 MPa) accident scenarios, which is not covered in this work.

Limited loss of flow experiments were performed at the JAEA 37 rod test facility at prototypical RBWR steady state operating conditions [19]. The tests showed that the measured post-CHF temperature is higher than the common models such as TRAC, which is also used in TRACE. Since outlet qualities of these tests are well over 40% with void fraction in excess of 80%, it is postulated that film boiling is initiated instead of transition boiling, therefore, smaller than expected heat is transferred from the wall to the fluid. The heat transfer logic was changed accordingly to represent such a modeling feature.

The new developed TRACE post CHF wall heat transfer model for the RBWR was validated against the JAEA tests database. In order to predict the time when dryout occurs, the MIT critical power (CP) correlation was used. The validation study resulted in a great agreement between the TRACE RBWR model and the experimental data in terms of peak cladding temperature, quench temperature, and time when dryout occurs and is recovered. A sample result with direct comparison to experimental data is shown in Fig. 5-2. As shown, the time when dryout starts is almost identical to the experimental data as well as the peak cladding temperature. The TRACE v5 critical power correlations predicts a 1000 ratio meaning the operating conditions of the tests are beyond their range of applicability. Interestingly, in this small test, the CHF lookup tables within TRACE predicted that the bundle will not reach post-CHF conditions.

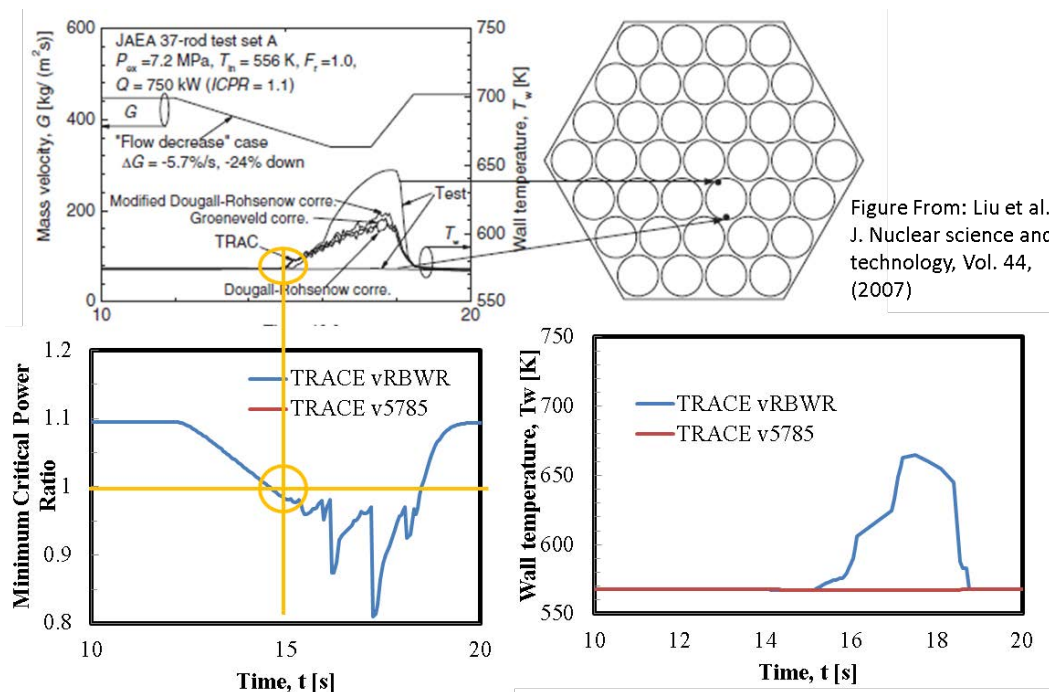


Figure 5-2. The comparison of JAEA experimental data [19] to the base TRACE (v5785) and improved TRACE (vRBWR).

5.1c Fuel Thermal Conductivity Model

The RBWR-AC and RBWR-TB2 fuel are loaded with a large concentration of plutonium oxide. In addition, both reactors are designed with high peaking factors due to the axial double-sandwich blanket and fissile design. The large peaking leads to a large variation in the local fuel burnup axially and radially in the core. The current version of TRACE does not incorporate burnup dependent thermal conductivity for MOX fuel. The FRAPCON MOX thermal conductivity model [20] is incorporated within TRACE, in order to provide an accurate prediction of the fuel temperature. The TRACE 3D burnup distribution in the core is taken from the PATHS/PARCS simulation.

5.1d RBWR TRACE Model

All 720 assemblies of the RBWR-AC and RBWR-TB2 are explicitly modeled in TRACE with axial nodalization similar to the PATHS/PARCS model. Such fine spatial nodalization allows the analysis to focus on the physics behind the safety and stability performance of such reactors in these first-of-kind simulations. Additional information on the TRACE model can be found in the following reference [21].

5.1e RBWR PARCS Model

The same PARCS model used for the PATHS/PARCS simulations was coupled to the TRACE model. PARCS [10] only performs a few initial iterations in order to converge the steady state and adjoint flux distribution and eigenvalue, upon initiation of the transient simulation. It was found that for the RBWR at least 300 iterations are required to obtain a converged steady state and adjoint flux distribution and eigenvalue. Additionally, during transient simulation, it was found that multiple TPEN iterations caused numerical divergence. In order to avoid such a situation, the code was internally limited to one TPEN update per time step. The default residual limits were still met by increasing the number of non-linear iterations.

Another area of concern that was raised during the transient calculations was the utilization of the adjoint flux, which is derived from the 2-group coarse mesh finite difference (CMFD) solution, to calculate the reactivity during the transient. The reactivity was found to be very sensitive to the number of iterations and residual tolerances. The importance of generating comprehensive 3D cross-section libraries was also highlighted during the transient simulations. The generation of 3D cross-sections requires a larger number of branch cases compared to the 2D methodology. However, its generation is computationally expensive and therefore, only a few branches were simulated for the RBWR designs. The effect of cross section branches on safety performance is discussed in the upcoming sections.

Lastly, the current PARCS code does not properly transmit fuel temperatures obtained from TRACE for cross-section processing as it includes the cladding temperature as well. This under prediction of fuel temperature was somewhat corrected by using a Doppler weighting factor of 0.1 instead of the recommended 0.7 [10].

5.2 Coupled Steady State Simulation

The steady state TRACE/PARCS simulation of the RBWR-AC and RBWR-TB2 was performed by restarting from the PATHS/PARCS converged solution for the equilibrium cycle. The comparison of the two simulation methods is shown in Table 5-1 for both BOC and EOC. As shown, there good agreement overall between the two simulations. The difference in the average fuel temperature is mainly due to the difference in the thermal conductivity models. As shown, the EOL peaking factors are milder even though the average fuel temperatures predicted by TRACE increase due to higher burnups. PATHS fuel thermal conductivity correlation is for UO_2 and is not dependent on burnup. The average moderator destiny differs more between PATHS and TRACE for RBWR-AC compared to RBWR-TB2, since for AC the LPG correlation is used, while for TB2 the EPRI (RELAP5) correlation is used by PATHS. In TRACE, the void fraction correlation is not a drift flux model and is used as an iterative variable in solving the governing two fluid equations [18]. TRACE void fraction predictions are very close to RELAP5 predictions, which for the TB2 results in a similar average core fluid density between PATHS and TRACE. While void fraction passing to PARCS from TRACE can be adjusted to a desired value, the LPG correlation is only valid for a limited range of conditions and such a modification was not implemented.

Table 5-1
The comparison of PATHS/PARCS to TRACE/PARCS simulations

Reactor	BOC		EOC	
RBWR-AC	PATHS	TRACE	PATHS	TRACE
Fuel T_{ave} (K)	807	1102	804	1133
Ave Fluid D (g/cm^3)	0.37	0.33	0.35	0.31
Core K_{eff}	0.9878	0.9813	0.9849	0.9794
Peak Assem. Factor	1.292	1.3202	1.225	1.2372
RBWR-TB2				
Fuel T_{ave} (K)	852	1084	848	1131
Ave Fluid D (g/cm^3)	0.32	0.34	0.28	0.29
Core K_{eff}	0.9874	0.9898	0.9842	0.9826
Peak Assem. Factor	1.220	1.252	1.230	1.259

The core-averaged axial power peaking factors of both cores were found to be in great agreement. The comparison of PATHS and TRACE for prediction of the RBWR-TB2 axial power factors is shown in Fig. 5-3.

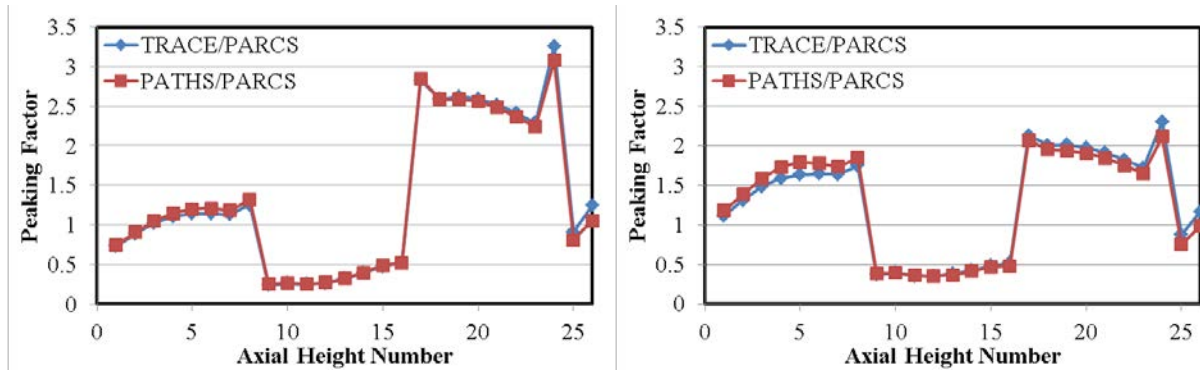


Figure 5-3. The core-averaged axial power peaking factor of RBWR-TB2 at BOC (left) and EOC (right).

One of the main motivations behind this study was to move away from traditional 2D reactor nodal methods and extend to 3D cross-section generation. Fig. 5-4 compares the RBWR-AC axial peaking factor based on both 2D cross sections (generated by the deterministic code HELIOS) and 3D cross sections (generated by the Monte-Carlo code SERPENT). As shown, the 2D cross-sections result in a large peak in the upper blanket region which is not seen in the 3D cross-section simulations. The 2D cross sections also predict a balanced power in the two fissile zones while the 3D cross-sections predict lower power in the upper fissile zone. Such a difference in the power distribution, as well as the isotopics, results in a more negative void reactivity feedback predicted by the 3D cross-sections.

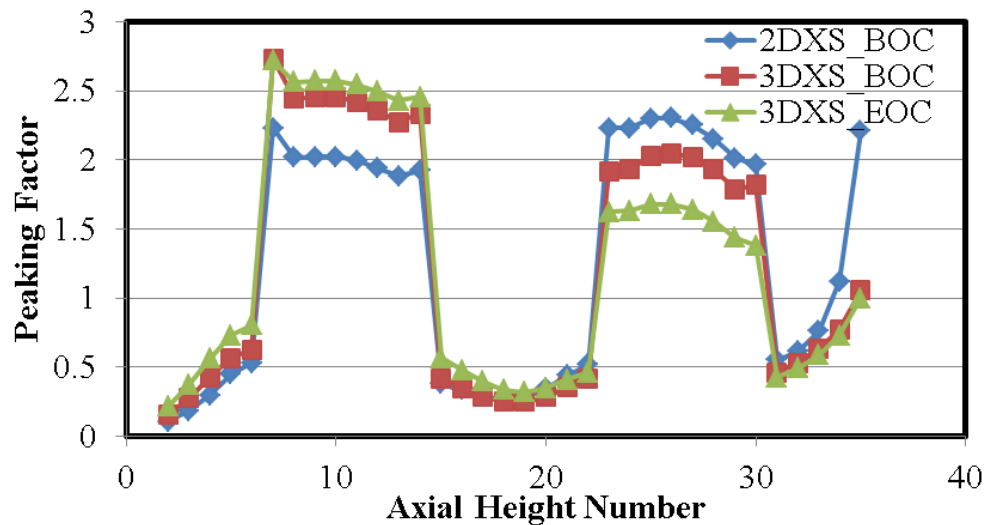


Figure 5-4. RBWR-AC axial power factor distribution.

Table 5-2 lists the minimum critical power ratio (MCPR) calculated by the MIT and HITACH CISE correlations. The table values imply that if the MIT correlation is used, there is a significant deficiency in the steady state CP margin that is typically required for safety analysis (>1.3).

Table 5-2
The MCPR for RBWR-AC and RBWR-TB2 designs (From TRACE/PARCS simulations)

MCPR	HITACHI	MIT
RBWR-AC	1.25	1.10
RBWR-TB2	1.40	1.05

Chapter 6: Safety and Stability Analysis

6.1 Safety Analysis

The all pump trip and loss of coolant accidents were identified as the limiting accidents by MIT [21] and HITACHI [22]. The higher quality and void fraction as well as smaller coolant volume in the RBWR type cores, reduces its thermal capacity and makes it susceptible to loss of flow and coolant accidents. In this study, the behavior of the core against the all pump trip accident is analyzed.

The sequence of events during the all pump trip accident is listed in Table 6-1, which is consistent with the ABWR all pump trip scenario [23].

Table 6-1
ABWR All pump trip sequence

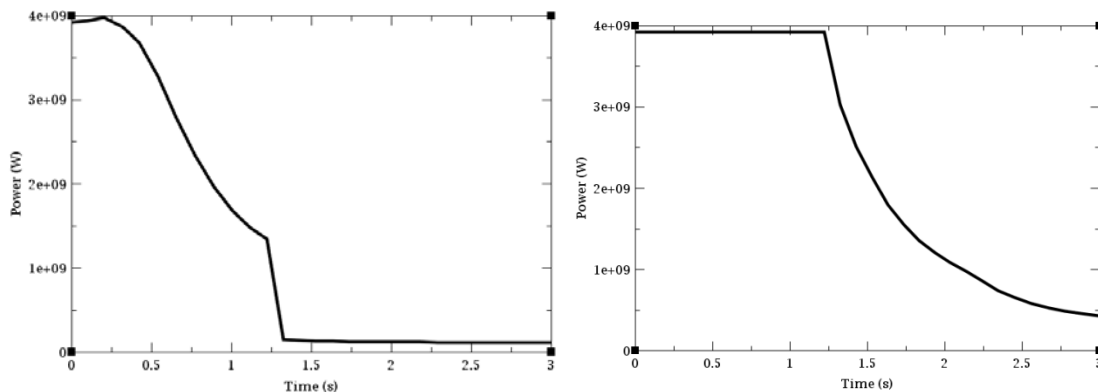
Time (s)	Event
0	Trip of all RIPs initiated
1.22	Reactor scram
1.85	Feed water flow pump trip
1.97	Turbine Trip initiates bypass operation
20	End of Simulation

The peak cladding temperature (PCT) is the most important parameter tracked during this accident. The PCT also dictates the equivalent cladding reacted (ECR), if the cladding temperature exceeds at least 1000 K. The typical safety limit imposed on Zircaloy cladding during a core uncover design basis accident is a temperature of ~ 1204 °C (2,200 °F), to avoid excess oxidation. The ECR is also typically limited to 17%, however, recent US regulation has moved toward a hydrogen dependent ECR [24].

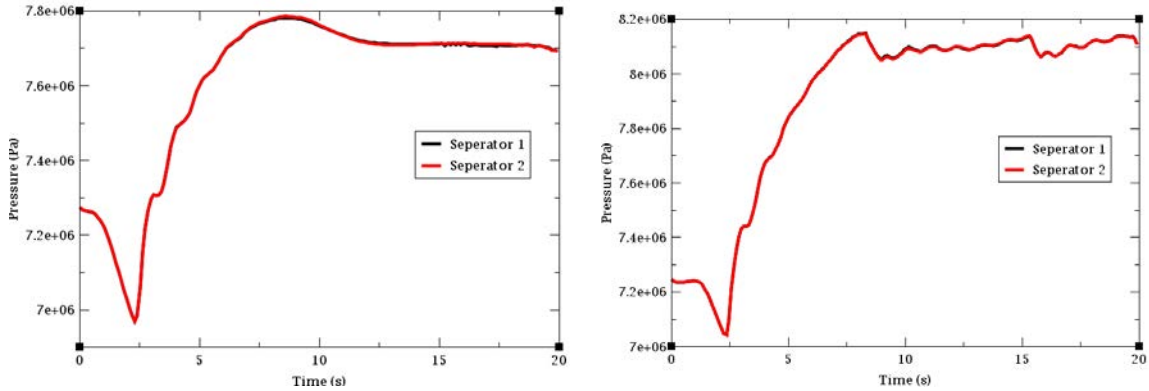
The introduction of a novel 3D cross-section library in order to perform full cycle depletion and transient analysis is still under further development. Therefore, sensitivity studies are performed in order to capture the behavior of the core response during the all pump trip accident. The following sensitivity cases are simulated:

- Simulation with no cross branch (“NCB”): The introduction of fully inserted control rod cross branches tend to bias the cross-section interpolation and result in a more negative reactivity feedback. The improvement of the cross branches are left as future work.
- Simulation with no feedback (“NFB”): One of the main goals of this study was to quantify the fuel and void reactivity feedback of the RBWR reactors. However, it has been shown that the magnitude of such reactivity is more sensitive to operating conditions and cross-section processing than typical BWRs. Therefore, a case assuming both the fuel and void reactivity are zero (e.g. zero power coefficient) is simulated in order to bound the performance of the RBWR during all pump trip accident, since the initial flow decrease should result in negative reactivity feedback according to steady state reactivity feedback calculations. For this simulation, point kinetics is used for a core with the power distribution derived from the coupled TRACE/PARCS simulation.
- Simulations with MIT and HITACHI CISE correlations at BOC and EOC.

Fig. 6-1 shows the transient power and reactor pressure vessel (RPV) pressure behavior for the RBWR-TB2 all pump trip accident for the NCB with MIT CP correlation and NFB with MIT CP correlation at BOC. As shown, the coupled simulation predicts a large negative reactivity, bringing the core power down considerably. As mentioned above, the magnitude of this decrease is exaggerated due to the limitation of the current PARCS simulator to calculate accurate dynamic feedback. As expected, the NFB case core power stays constant until the SCRAM set point is reached. The RPV pressure is increased by ~ 0.9 MPa for the NFB case, which is very close to the conventional ABWR transient response [23].



(a)



(b)

Fig. 6-1. The transient (a) power and (b) RPV pressure response for RBWR-TB2 NCB (left) and NFB (right) with MIT CP correlation at BOC.

Fig. 6-2 shows the separator inlet mass flow rate for the same transients. Each separator is connected to one half of the core and a thermal hydraulic instability is observed for both the NCB and NFB after the initial flow reversal is observed.

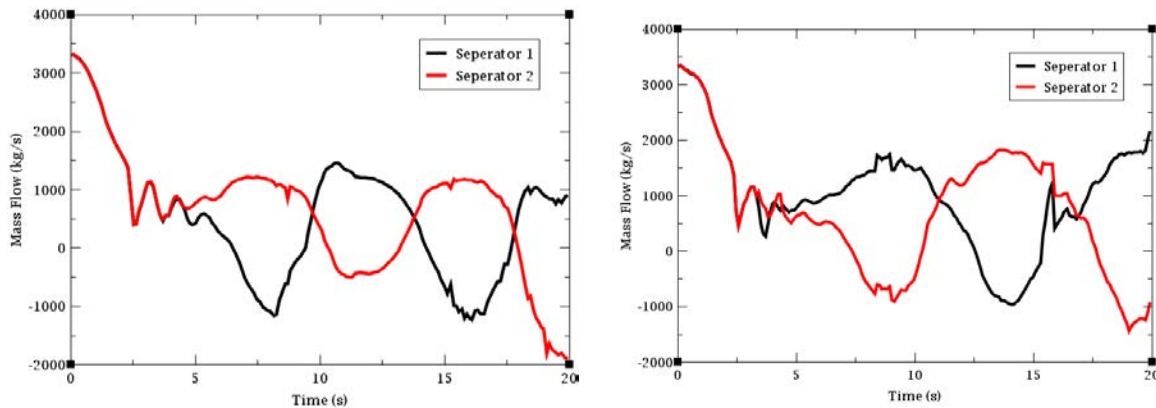


Fig. 6-2. The transient separators' inlet mass flow rate response for RBWR-TB2 NCB (left) and NFB (right) with MIT CP correlation at BOC.

The inlet mass flow rate and outlet void fraction of the hot assembly where PCT occurs for the RBWR-TB2 design at both BOC and EOC are shown in Fig. 6-3. The hot assembly is situated radially toward the core periphery, with BOC peaking factor of 1.25 and burnup of ~16 MWd/kgHM. It is noted that the RBWR-AC response to this transient is similar to the RBWR-TB2.

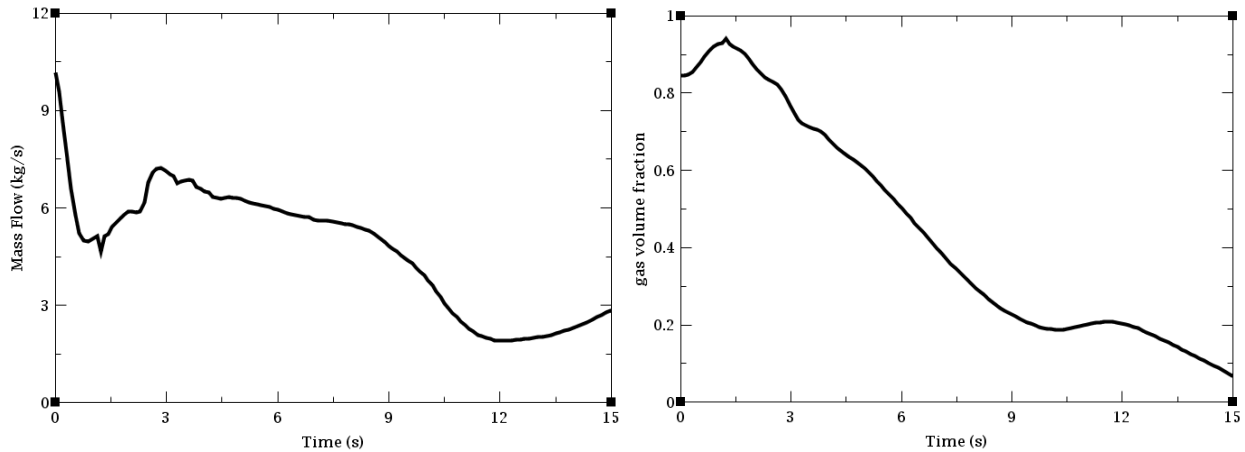


Figure 6-3. The transient inlet mass flow rate (left) and outlet void fraction (right) response for RBWR-TB2 NCB with MIT CP correlation at BOC.

One of the fundamental differences between the coupled and point kinetics analysis is that the individual assembly axial power distribution as well as the core radial power distribution change for the coupled analysis based on the operating conditions while the point kinetics steady state spatial power distribution is held constant throughout the transient. Fig. 6-4 shows that based on the core-averaged axial power peaking factor, the point kinetics simplification is quite acceptable, since the axial power shape does not change significantly.

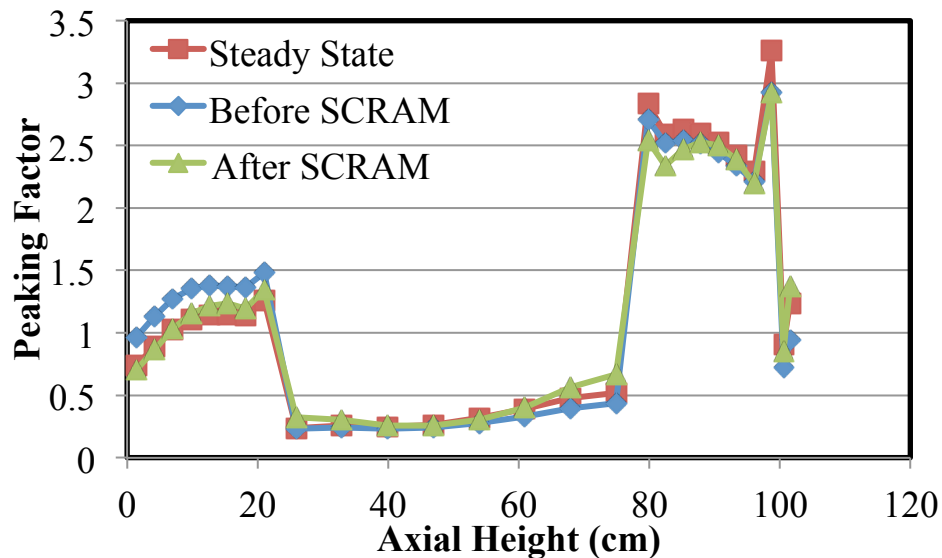


Figure 6-4. The core-averaged axial peaking factor for RBWR-TB2 NCB with MIT CP correlation at BOC.

The PCT during the all pump trip simulations performed for the RBWR-AC and RBWR-TB2 is shown in Fig. 6-5. As expected, the MIT correlation predicts a higher or same PCT compared to the HITACHI correlation, since it predicts a lower CP margin for both RBWRs. As shown, on average, the RBWR-TB2 results in a higher PCT than the RBWR-AC. The NFB cases for TB2 yield the highest PCTs, implying a negative void coefficient. The removal of the cross branches result in a less negative void coefficient and therefore a higher PCT, as shown in Fig. 6-5. In general, at EOC, the PCT is higher for both the TB2 and AC even though the peak linear heat generation rate is smaller. In fact, the AC EOC PCT is larger than its equivalent NFP case. This implies that an overall positive reactivity has been inserted during the transient. This can be explained since at EOC, the PATHS/PARCS calculated void reactivity for the AC is very small (~ 10 pcm/%void) using the RELAP5 void fraction correlation. The overall numerical error in calculating reactivity also contributes to this result. A similar trend is observed for the simulation with the 2D HELIOS cross-sections, where PCT is larger than the NFB case due to its positive void coefficient. Nevertheless, all the calculated PCTs are well below the safety limit of ~ 1480 K. Similarly, the maximum ECR was 0.18% for the TB2 with NFB at EOC, which is well below the 17% limit. For a typical ABWR, the PCT is ~ 800 K [23], which is on par with most of the coupled simulation results.

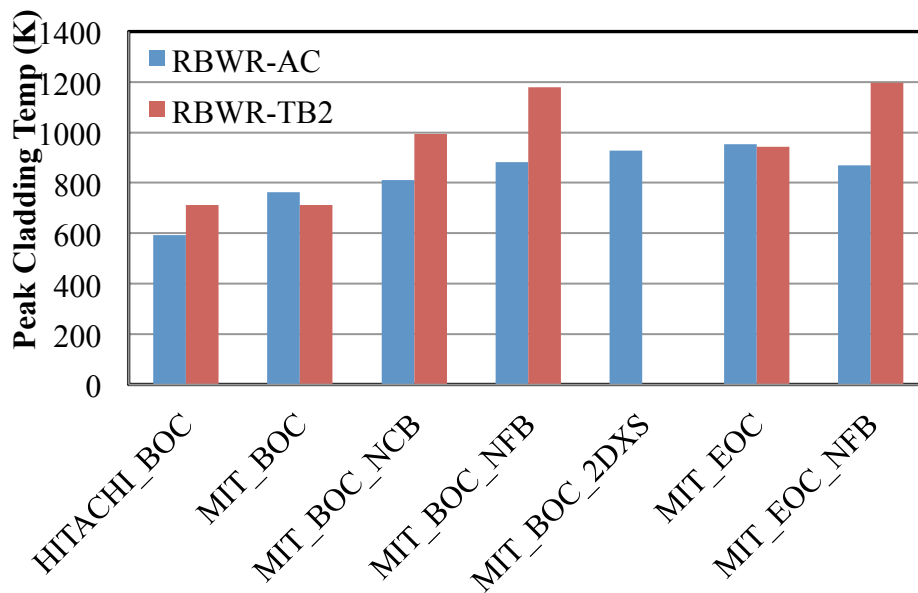
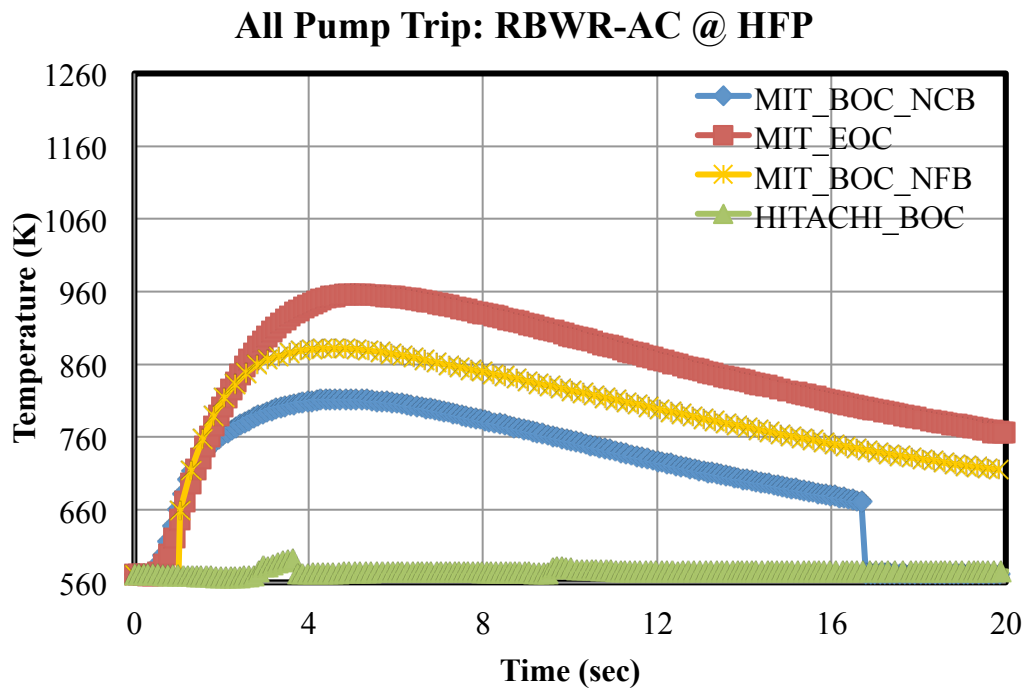
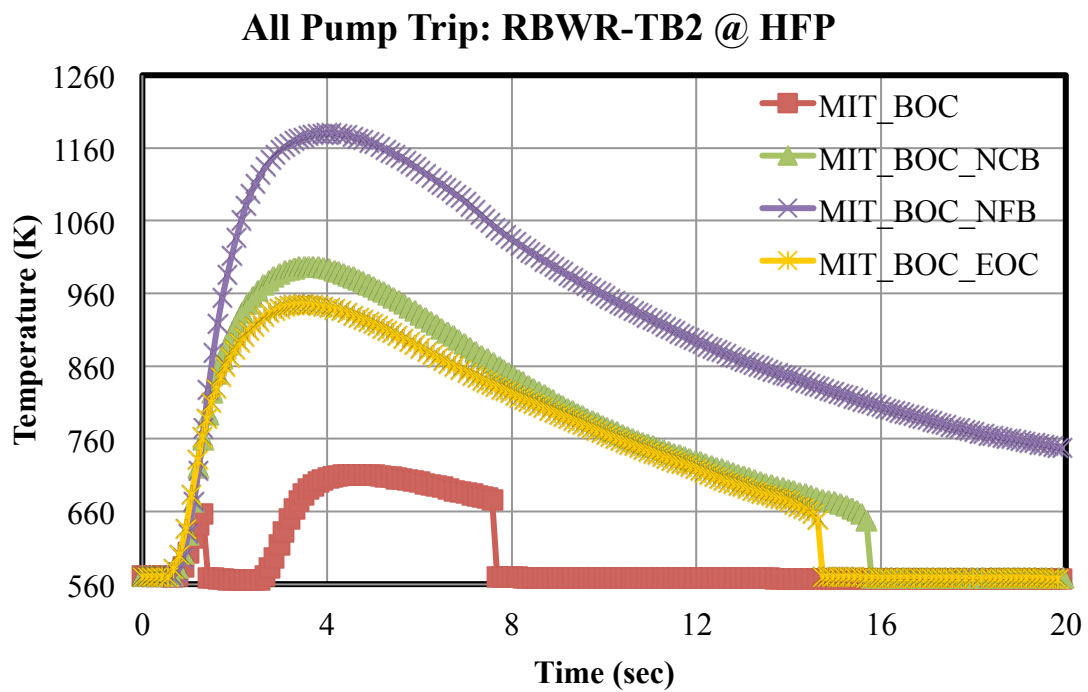


Figure 6-5. The PCTs during all pump trip accident simulations.

The evolution of PCT as a function of time is shown in Fig. 6-6 for both the AC and TB2 for selected transients. For all coupled simulations, the PCT goes through quenching within the simulated 20 seconds.



(a)



(b)

Figure 6-6. The PCT evolution during the all pump trip accident for (a) RBWR-AC and (b)RBWR-TB2.

6.2 Stability Analysis

Any BWR type system will have susceptibility to two phase flow oscillations of the density wave type. There are three oscillation modes in BWR density wave stability analysis that are commonly investigated. They are: core-wide in-phase or global instability, region-wide out-of-phase instability and single channel thermal hydraulic instability without feedback. All three modes were shown to not be of concern for both RBWRs using the frequency domain approach [21]. This study focuses on assessment of the global and regional stability with the coupled time domain approach.

Table 6-2 summarizes parameters that are different for the RBWR designs compared to the ABWR design and its expected effect on stability.

Table 6-2

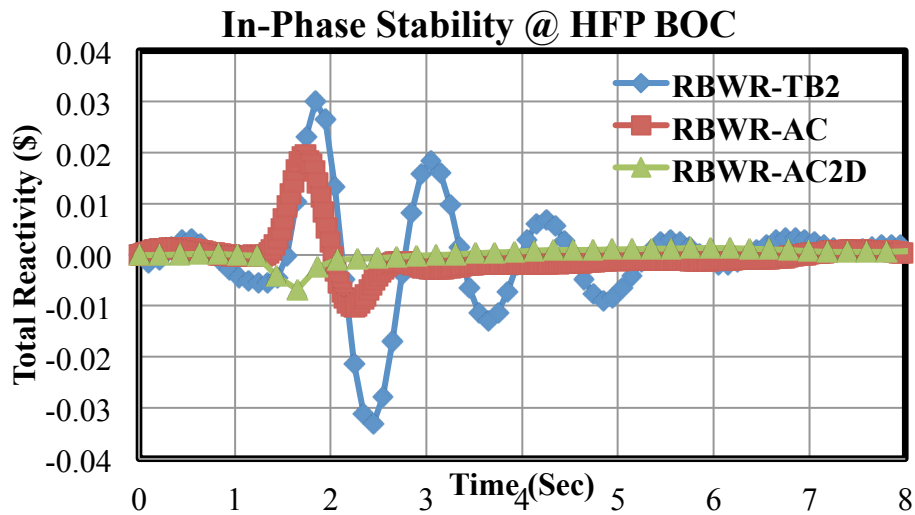
The summary of parameters governing the differences between ABWR and RBWR-AC/TB2 stability performance (+/- means more/less stable; * means either possibility).

Parameters	ABWR	RBWR-AC/TB2	Effect
Fuel Height (m)	3.7	1-1.3	+
Pressure Drop (kPa)	130	70-100	*
Core Exit Quality (%)	14.5	35-40	-
Spacer Grid Span (cm)	~50	24.5	-
Fuel Height to Core Outer Diam. Ratio	~0.7	~0.2	-
Fuel Time Constant (sec)	6	~5	-
Average (Peak) Heat Flux (kW/m ² -s)	440 (1036)	471 (1412)	-
Subcooling (°C)	10	5	*
Effective Delayed N Fraction x 10 ⁻³	6-5	< less	-
Coolant Average Void Fraction (%)	~40	~60	-
Void coefficient (PCM/% void)	-130 to -70	-50 to -15	+
Inlet Orificing	15-20	30-70	+

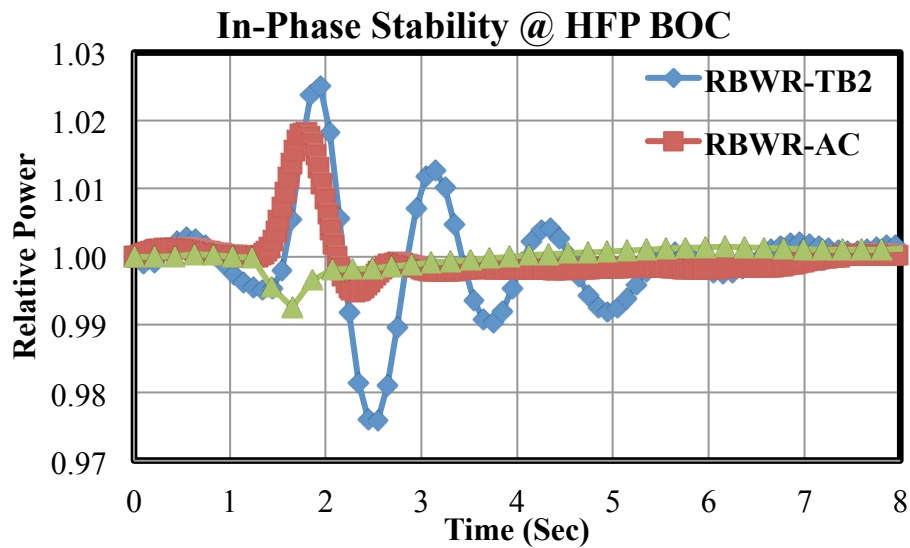
6.3a Global Mode

To assess the RBWR designs' performance against the global stability mode, a positive pressure perturbation from the turbines were simulated to uniformly collapse the vapor voids in the core. Since both RBWRs exhibit negative void coefficients of reactivity, an increase in pressure should lead to an initial increase in power. The increase in power is expected to be followed by a decrease in power since the initial increase results in more voids, leading to negative reactivity. Fig. 6-7 shows the total reactivity and relative power response to such perturbation. The simulations were performed at HFP and BOC. The RBWR-AC with 2D

HELIOS cross-sections was also included and as expected, it resulted in an initial power decrease due to its positive void reactivity. Both the RBWR-TB2 and AC have <0.5 decay ratios, implying stable performance. The RBWR-AC shows a very stable behavior which is somewhat expected from its much lower void coefficient (-40 vs. -20 pcm/%void). This also implies the stability performance of such a reactor is very sensitive to the void coefficient magnitude.

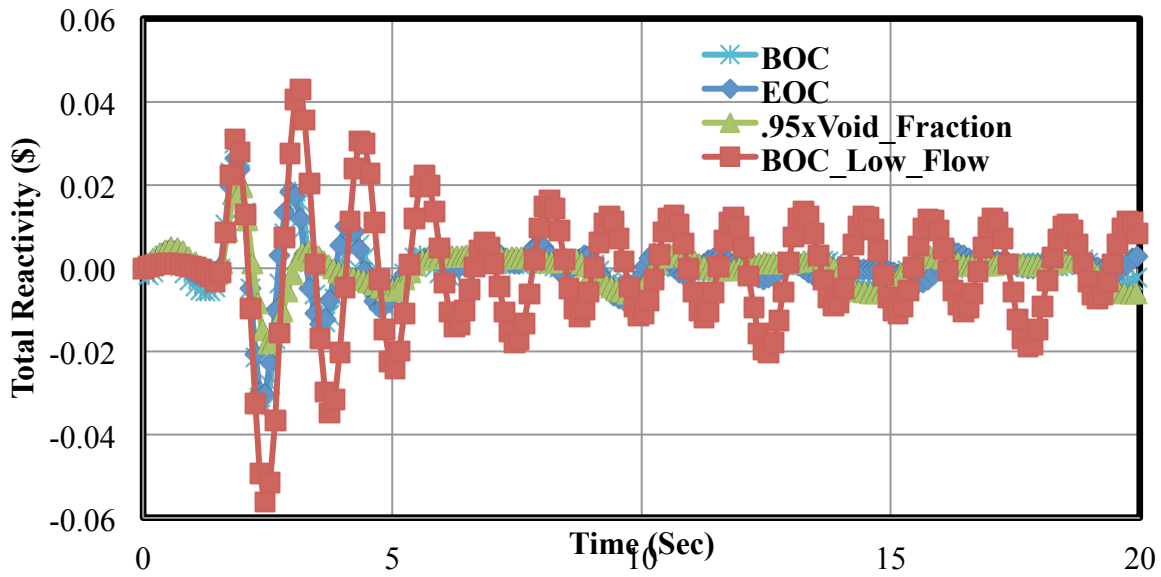


(a)

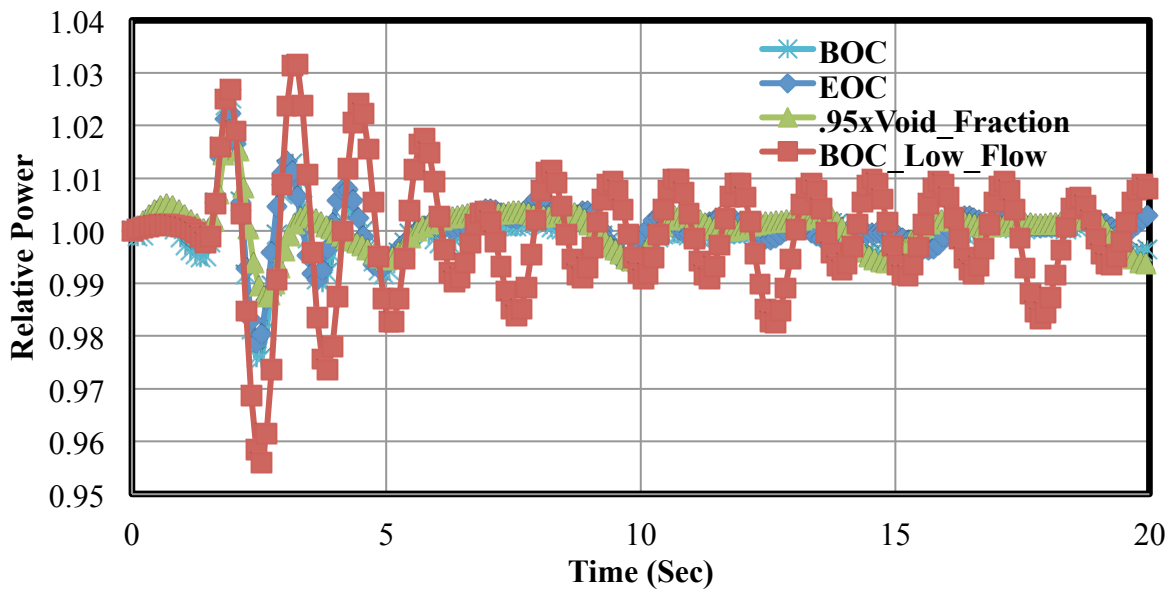


(b)

Figure 6-7. The oscillation of (a) reactivity and (b) power due to a pressure perturbation.



(a)



(b)

Figure 6-8 The oscillation of (a) reactivity and (b) power due to a pressure perturbation for RBWR-TB2 at HFP.

Since the RBWR-TB2 performance resulted in a higher decay ratio than the AC, a sensitivity study on TB2 stability performance is desired. Fig. 6-8 shows the total reactivity and relative power for a similar simulation as Fig. 6-7, in addition to an EOC case, 90% flow case and a case where the void fraction in all coolant channels has been multiplied by 0.95 (e.g. reduced void fraction case). A similar decay ratio is observed at both BOC and EOC. At EOC, the void

coefficient is slightly decreased (42 to 37 pcm/%void) for TB2, however, the core average void fraction is increased by 7% compared to BOC. Since the radial peaking factor remains relatively unchanged, the stabilizing effect of a smaller void coefficient is offset by a higher average void fraction. For the reduced void fraction case, a large sensitivity is observed as the core shows a very stabilizing response to the perturbation with a 5% decrease in its void fraction. On the other hand, 90% flow where the core average void fraction is increased by 3% results in a significantly higher decay ratio (~ 0.75 - 0.8). Also, the oscillations do not dampen out as regional oscillations (as discussed in the next section) continue. The regional oscillations do not seem to grow and seem to slowly damp out. It is worth noting that the RBWR-TB2 with 100% flow at HFP does not have sufficient CP margin and at 90% flow, the CPR margin will further degrade. In other words, while the simulations show the RBWR-TB2 could be susceptible to global mode of instability, it is expected that the RBWR-TB2 will be redesigned in order to meet sufficient CP margin.

6.3b Regional Mode

The core out-of-phase perturbation is simulated by initiating control rod bank movements in only 1/3 of the core section. The selected control banks are removed by 10 steps from 1 to 1.5 seconds and moved back to their original positions between 1.5 to 2 seconds of the simulation time. The RBWR has a larger diameter-to-height ratio compared to the ABWR and regional instabilities could be observed. Fig. 6-9 shows such a perturbation for the RBWR-TB2 and AC at HFP and BOC. A similar trend to the in-phase perturbation is observed, as both core performances imply a very stable response to this mode of stability.

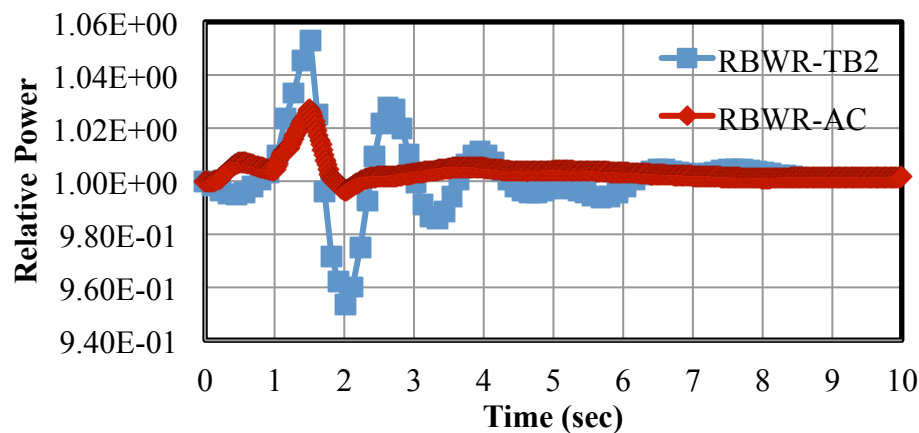


Figure 6-9. The relative core power for RBWR-TB2 and AC during core out-of-phase perturbation at HFP and BOC.

As shown by Fig. 6-10, similar to the global mode performance, the 90% flow case for the RBWR-TB2 resulted in a slow decaying of the initial oscillations and a persistent continuing small oscillation. The nature of the long lasting oscillation is further investigated via core radial power maps.

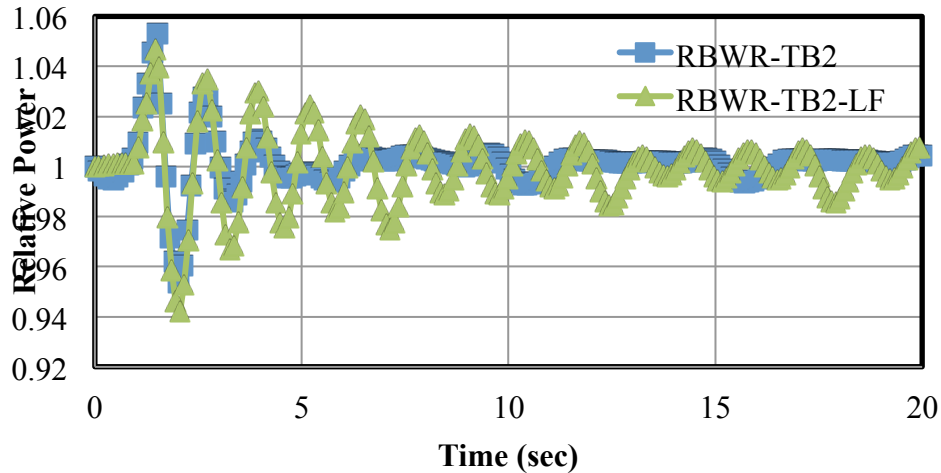
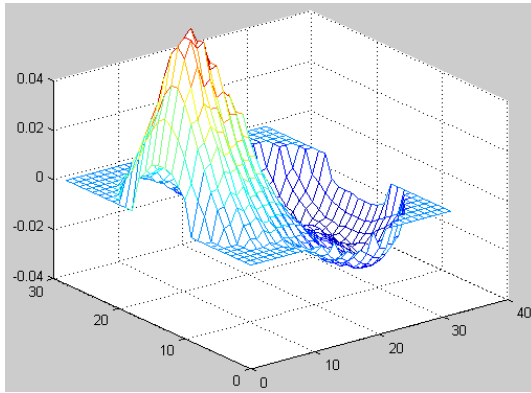
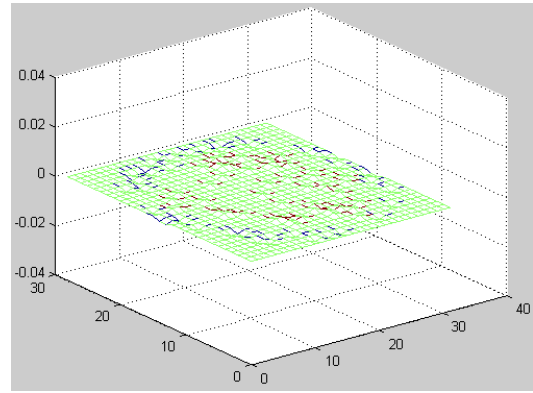


Figure 6-10. The relative core power for RBWR-TB2 at 100% and 90% flow during core out-of-phase perturbation at HFP and BOC.

As shown in Fig. 6-10, the initial perturbation decays out and yields a uniform core power for the RBWR-TB2 after 7 seconds for the nominal 100% flow case. However, as shown in Figure 6-11b, the perturbation in one third of the core transforms to a radial regional oscillation where the outer region of the core is out-of-phase with the inner region. The main factor causing such an oscillation in the radial shape is the unique orificing pattern of the RBWR designs. Unlike the ABWR, where two orificing groups are used, there are five groups in the RBWR-TB2 that are not necessarily positioned at the core periphery. Nevertheless, at 19 seconds after the initial control rod perturbation the core power distribution is close to its initial distribution since the regional radial oscillation slowly decays.

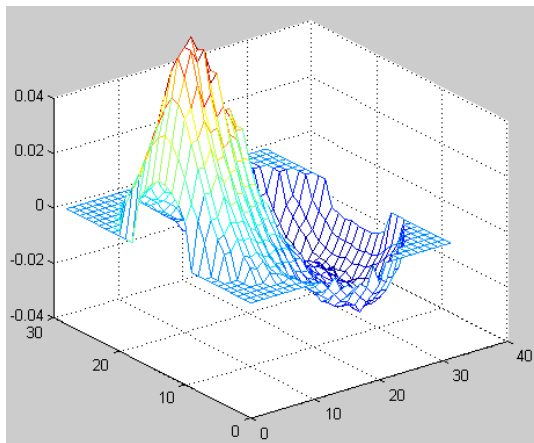


1.5 sec

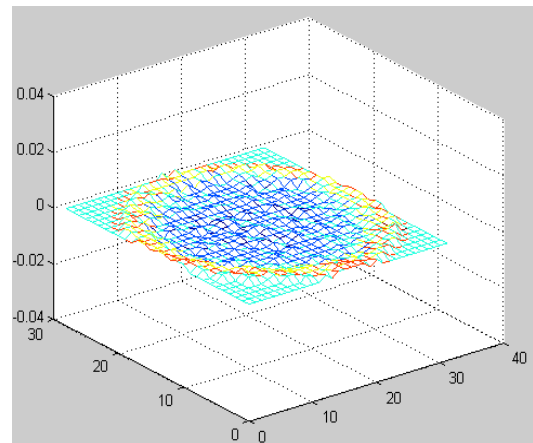


7 sec

(a)

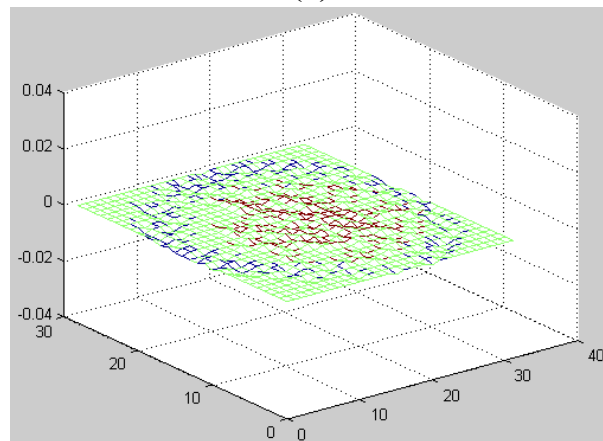


1.5 sec



7 sec

(b)



19 sec

(b cont.)

Figure 6-11. The radial power distribution of RBWR-TB2 subtracted from the steady state distribution for the core out-of-phase perturbation at (a) 100% flow and (b) 90% flow cases at HFP and BOC.

Chapter 7: Summary

7.1 PARCS/PATHS Equilibrium Cycle

This work solved some of the challenges associated with modeling an axially heterogeneous, mixed-spectrum reactor with an innovative approach to the conventional two-step method for LWR analysis. The work showed that 2D lattice methods were not sufficient to generate cross sections for this problem because the underlying assumption of no net current in the vertical direction breaks down at the interfaces between enriched plutonium seed and natural uranium blanket regions of the core, and also due to strong variation of the moderator density in the axial direction. Cross sections were generated with a 3D single assembly model, instead of a 2D lattice, in order to capture the important effects of axial streaming in this core. Axial discontinuity factors were also generated to help the 3D nodal diffusion solution better match the 3D Monte Carlo results. This was one of the significant original advances resulting from the research.

The equilibrium RBWR core was obtained iteratively by simulating depletion cycles with PARCS/PATHS. The LPG void correlation, which was found to be appropriate for tight-pitch BWRs like the RBWR-AC [14], was added to PATHS. This correlation was necessary to obtain the correct void distribution, which has a significant effect on the void reactivity coefficient. The void coefficient was negative for the RBWR-AC and RBWR-TB2 designs.

The main objectives of both designs were confirmed by the equilibrium cycle analysis. The fissile inventory ratio of the RBWR-AC was calculated to be slightly greater than 1, allowing for self-sustenance of fuel, including some small loss in reprocessing. The TB2 analysis showed that it was quite effective at burning TRUs, with a calculated fission efficiency of 44.3% (i.e. 44.3% of heavy metal fissioned was TRU).

While the designs performed well in many respects, the large power peaking in the fissile fuel zones produced very high discharge burnups which were beyond the capabilities of standard oxide fuels. This is one of a few reasons that the designs, as they were analyzed in this work, will require redesign and additional investigation to meet all criteria for safe operating conditions.

7.2 PARCS/TRACE Transient and Stability Simulations.

The first-of-kind coupled transient simulation of the RBWR designs were performed with the TRACE/PARCS code package. The code package had to be improved in several areas in order to effectively model the dynamic performance of RBWR type systems. The steady state simulation of the reactors confirmed the previous analytical estimates [14] that using the more reliable MIT-CISE correlation results in too low of a CP margin as redesigns of both the RBWR-AC and TB2

are required. The meeting of steady state CP margins remains the most important issue to be addressed in future analysis.

The safety analysis focused on the all pump trip accident, which is assumed to be the most limiting design basis accident for the RBWR designs. It was found that the 3D cross section libraries require further expansion and improvements. Thus, sensitivity studies were performed to compensate for this uncertainty. It is concluded that both the RBWR-TB2 and AC are expected to perform safely during the all pump trip accident. Though, the RBWR-AC at EOC featured a positive void reactivity which increases the complexity of its design licensing process. It was found that the coupled simulations do not significantly add value to the analysis as the point kinetics calculations were able to capture the performance of the design sufficiently. The improvement in the dynamic reactivity methodology of PARCS remains the most important area for future work in terms of future methods development.

The stability analysis highlighted the large sensitivity of RBWR designs to both the void fraction and void coefficient. However, at nominal operating conditions, both designs are expected to not suffer with global and regional modes of oscillation. The complex orificing and higher diameter-to-height ratio are believed to be the cause of small but very slow decaying radial regional instabilities observed with the RBWR-TB2 at 90% rated flow. Future work needs to extend the analysis to other power-to-flow ratios in order to determine the operating map of the RBWR designs. However, further improvements in the cross-section library are required and thus, it is left as future work.

Following is a brief summary of the accomplishments of this project:

- Re-evaluation of all the experimental data available for the RBWR flow regime and recommendation of the best correlation for void fraction prediction and CP prediction
- Development of performance analysis capability for hard spectrum BWRs
- Development of a high-fidelity 3-D core simulator (Serpent-PARCS-PATHS) that is capable to accurately account for strong axial heterogeneities, axial leakage and spectral change across the core
- Development of a time-dependent core simulator (modified PARCS-TRACE) for transient, stability and accident analysis for non-orthogonal geometries
- Confirmation of a negative void reactivity coefficient for both the RBWR-AC and RBWR-TB2 designs
- Elucidated issues with the critical power ratio for both designs, especially the RBWR-TB2
- Potential safety concerns (i.e. high power peaking) indicate the core designs will need some modification

REFERENCES

1. R. TAKEDA et al., “BWRs For Long-Term Energy Supply And For Fissioning Almost All Transuraniums,” Global 2007, Boise, Idaho, September 9-13 (2007).
2. M. Kazimi, T. Downar and E. Greenspan, “Safety Evaluation of the RBWR – a Hard Spectrum Boiling Water Reactor Design,” EPRI Final Report, May, 2009
3. Robert Hill, Personal Communication, December, 2010.
4. J. LEPPÄNEN, “PSG2 / Serpent – A Continuous-energy Monte Carlo Reactor Physics Burnup Calculation Code,” <http://montecarlo.vtt.fi> (2009).
5. Technical Evaluation of the HITACHI Resource-Renewable BWR (RBWR) Design Concept. EPRI, Palo Alto, CA: 2012. 1025086.
6. Brown, Nicholas. *3D Branching*. Personal Correspondence. BNL (2012).
7. B. HERMAN, E. Shwageraus, B. Forget and M.S. Kazimi, “Cross Section Generation Strategy for High Conversion Light Water Reactors,” MIT-NFC-TR-126, CANES, MIT (2011).
8. Y. Xu and T. Downar, “GenPMAXS-V5, Code for Generating the PARCS Cross Section Interface File PMAXS,” University of Michigan (2009).
9. K. SMITH, “Assembly Homogenization Techniques for Light Water Reactor Analysis,” *Progress in Nuclear Energy*, Vol. 17, No. 3, pp. 303-335 (1986).
10. T. Downar, Y. Xu, V. Seker, “PARCS, U.S. NRC Core Neutronics Simulator,” University of Michigan (2009).
11. “FAST: An advanced code system for fast reactor transient analysis”, *Annals of Nuclear Energy* 32, 1613-1631, (2005).
12. A. Wysocki, Y. Xu, B. Collins, A. Manera, T. Downar, “PATHS: PARCS Advanced Thermal Hydraulic Solver,” University of Michigan (2012).
13. M. Ishii, T. Hibiki, “Thermo-Fluid Dynamics of Two-Phase Flow,” Springer, New-York (2006).
14. K. Shirvan, N. Andrews, M. Kazimi, “Best Estimate Void Fraction and Critical Power Correlations for Tight Lattice BWR Bundles,” ICAPP, Korea, (2013).

15. "UM scope of work for the Hitachi RBWR project in 2014 JFY" Hitachi. (Document 2014-002-01) Aug, 2014.
16. "Resource-Renewable BWR for Long-term Energy Supply and Effective Use of Transuranic Elements," RBWR-Ph3-001 (2010).
17. "Resource-Renewable BWR for Effective Use of Transuranic Elements," RBWR-Ph3-002 (2010).
18. US NRC, "TRACE V5.0: Theory Manual," Division of Safety Analysis, Washington DC, 2012.
19. W. Liu, M. Kureta, H. Yoshida, H. Tamai, A. Ohnuki and H. Akimoto, " Critical Power Characteristics in 37-rod Tight Lattice Bundles under Transient Conditions," Journal of Nuclear Science and technology, 44, no. 4, pp. 1172-1181 (2007).
20. K.J. Geelhood, W.G. Luscher, C.E. Beyer, "FRAPCON-3.4: A Computer Code for the Calculation of Steady-State Thermal-Mechanical Behavior of Oxide Fuel Rods for High Burnup," Pacific Northwest National Laboratory, NUREG/CR-7022, Vol 1, 2011.
21. K. Shirvan et al., "Stability and Safety analysis of Tight Lattice Breeding LWR," Proceedings of ICAPP, 14276, 2014.
22. R. Takeda, M. Aoyama, M. Moriwaki, S. Uchikawa, O. Yokomizo, K. Ochiai, "General Features of Resource-Renewable BWR (RBWR) and Scenario of Long-term Energy Supply," *Proc. of International Conference on Evaluation of Emerging Nuclear Fuel Cycle Systems*, p. 938 (1995).
23. GE, "ABWR Design Control Document/Tier 2", Available from NRC.gov, (2007).
24. Raynaud P., Bielen A., "Cladding Hydrogen based Regulations in the United States," Water Reactor Fuel Performance Meeting, T3-031, Chengdu, China, 2011.

Appendix A

A comparison between Serpent, PARCS without ZDFs, and PARCS with ZDFs was done to demonstrate the necessity and effectiveness of using ZDFs to reproduce the Monte Carlo solution in PARCS. A plot of the axial flux variation was presented in the paper for a representative fast and thermal group. This appendix contains the rest of the data from that study. The normalized axial flux for each energy group for each of the three methods. Fig. A.1 shows the axial divisions and the pin lattice for the benchmark problem.

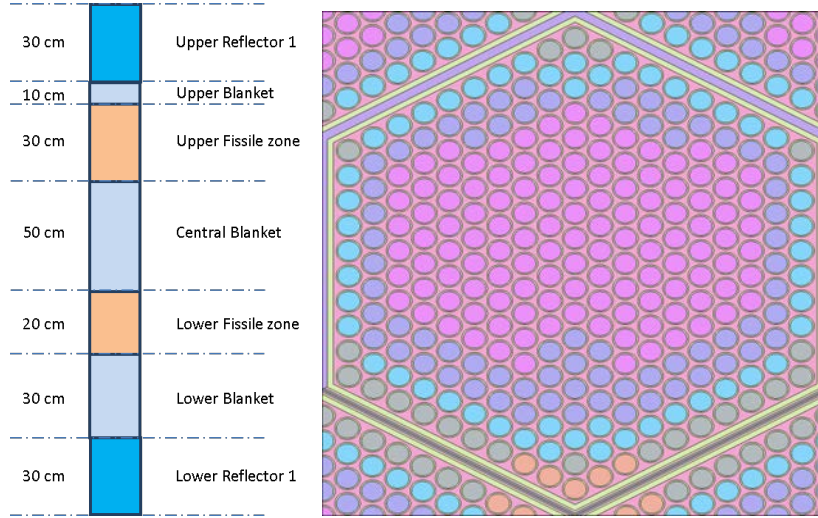


Figure A.1: RBWR Assembly Model

Table A.1: Comparison of Methods for a 12 Group, Full Assembly Problem

Method	K	Difference from Serpent (pcm)
3D Serpent	1.09601	-
3D PARCS without ZDFs	1.08772	829
3D PARCS with ZDFs	1.09601	0
3D PARCS with ZDFs no Diffusion treatment	1.09645	44

In all cases, PARCS is closer to Serpent with the ZDFs than without them. The PARCS solution without ZDFs significantly underestimates the flux in the lower fissile region in all 12 groups. Note that the vertical axis is different for all 12 figures. The energy group structure is given in Table A.2.

Table A.2: RBWR Multigroup Energy Structure

Energy Group	Upper Bound (eV)	Energy Group	Upper Bound (eV)
1	1.00E+07	7	4.09E+04
2	3.68E+06	8	5.53E+03
3	2.23E+06	9	1.30E+02
4	1.35E+06	10	3.93E+00
5	4.98E+05	11	1.45E+00
6	1.83E+05	12	6.25E-01

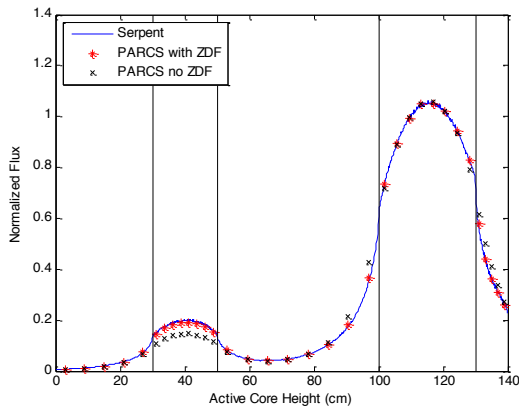


Figure A.2: Comparison of Serpent/PARCS for Group 1 Flux

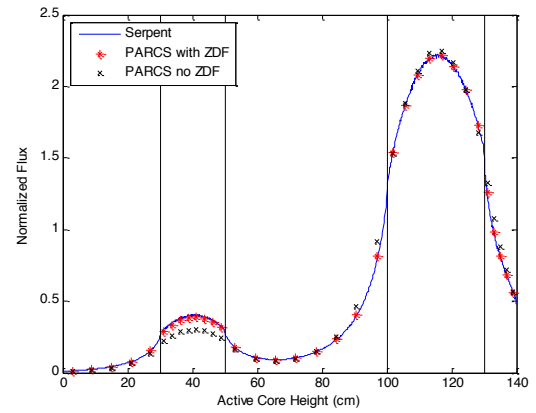


Figure A.4: Comparison of Serpent/PARCS for Group 3 Flux

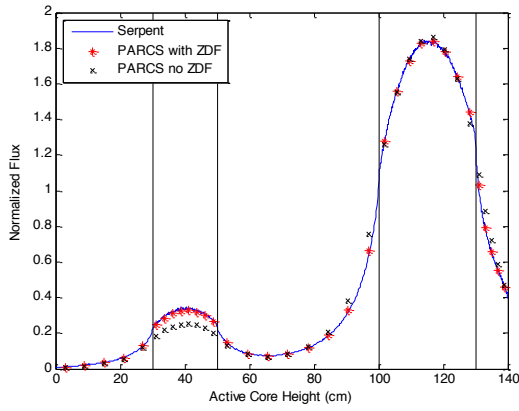


Figure A.3: Comparison of Serpent/PARCS for Group 2 Flux

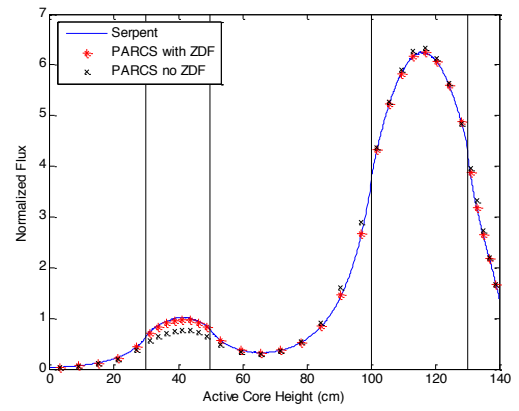


Figure A.5: Comparison of Serpent/PARCS for Group 4 Flux

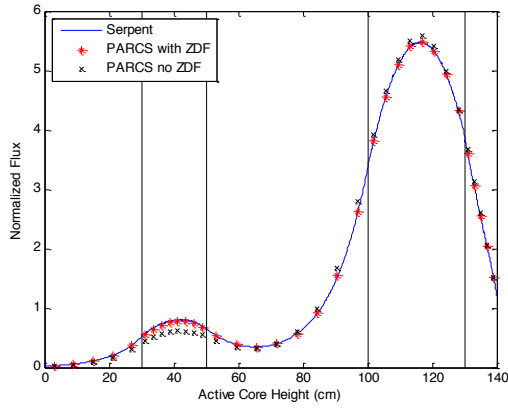


Figure A.6: Comparison of Serpent/PARCS for Group 5 Flux

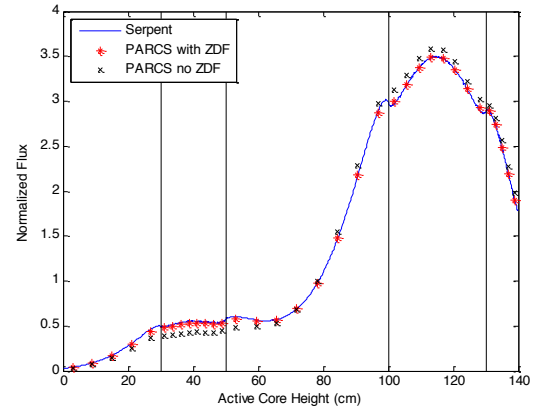


Figure A.9: Comparison of Serpent/PARCS for Group 8 Flux

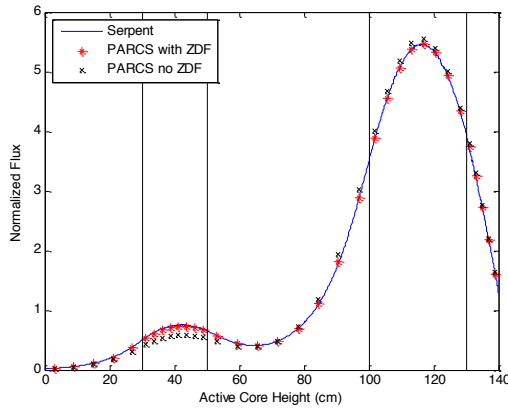


Figure A.7: Comparison of Serpent/PARCS for Group 6 Flux

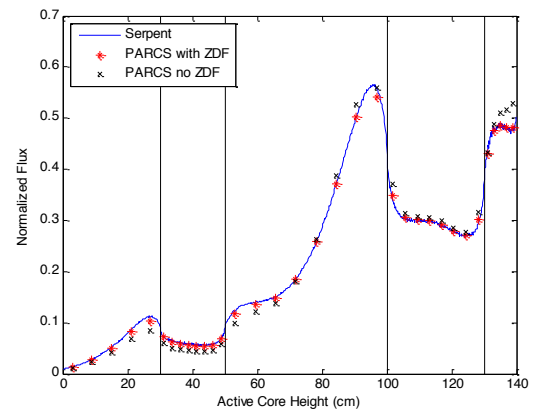


Figure A.10: Comparison of Serpent/PARCS for Group 9 Flux

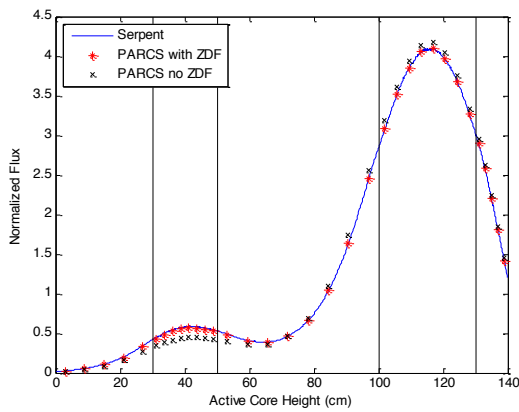


Figure A.8: Comparison of Serpent/PARCS for Group 7 Flux

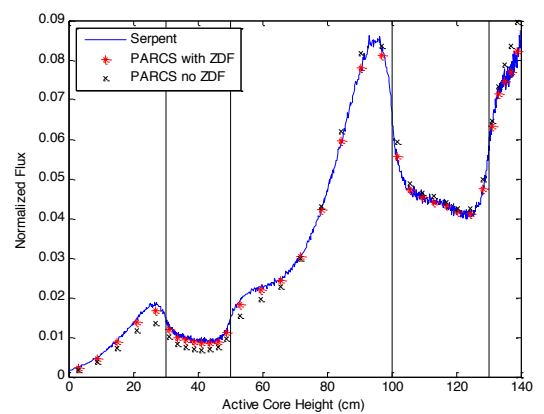


Figure A.11: Comparison of Serpent/PARCS for Group 10 Flux

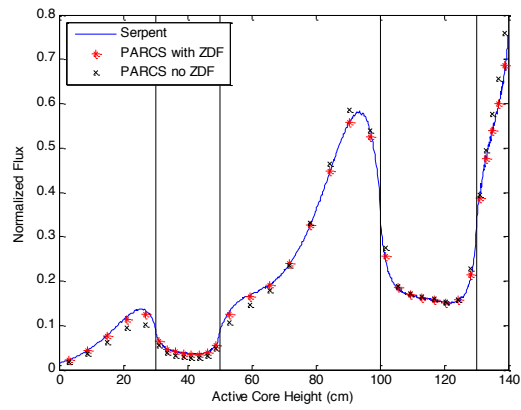


Figure A.12: Comparison of Serpent/PARCS for Group 11 Flux

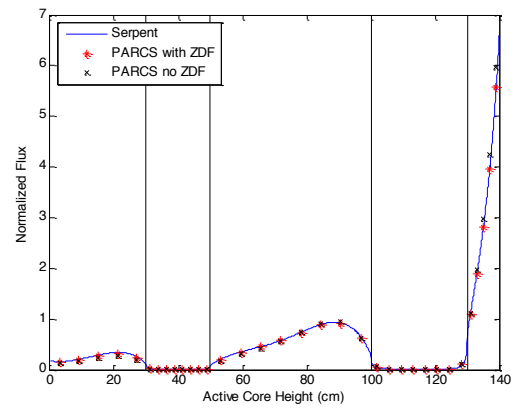


Figure A.13: Comparison of Serpent/PARCS for Group 12 Flux

Appendix B

A study of the integral perturbation method for generating 3D cross sections was performed by Brookhaven National Laboratory and is illustrated below. The results show that the integral assembly method produces a different flux spectrum. The differences are more pronounced for the coolant density branches at the top of the core, where the void fraction is changing rapidly. The fuel temperature branches show much less spectral difference between the two methods, which is why realistic coolant density distributions were used in Serpent, but realistic fuel temperature distributions were not necessary.

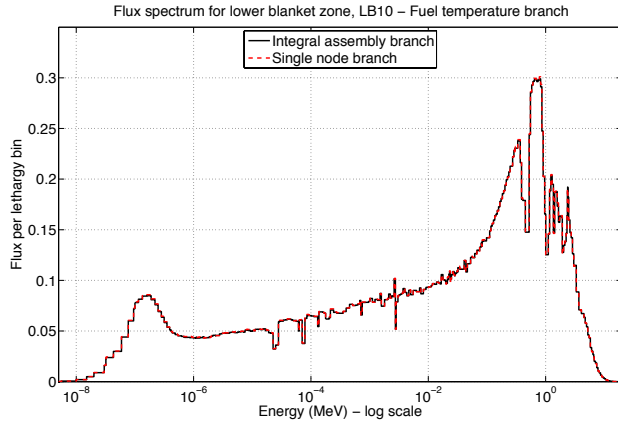


Figure B.1: Comparison of Spectra for Fuel Temperature Perturbation Methods, Lower Blanket

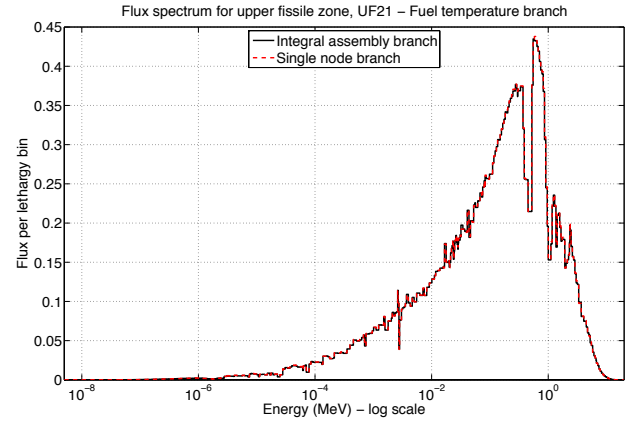


Figure B.3: Comparison of Spectra for Fuel Temperature Perturbation Methods, Upper Fissile

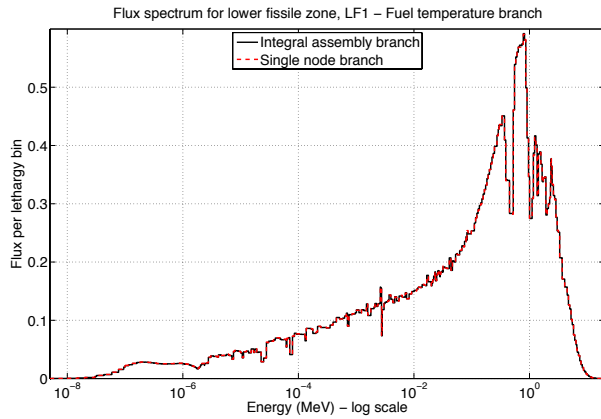


Figure B.2: Comparison of Spectra for Fuel Temperature Perturbation Methods, Lower Fissile

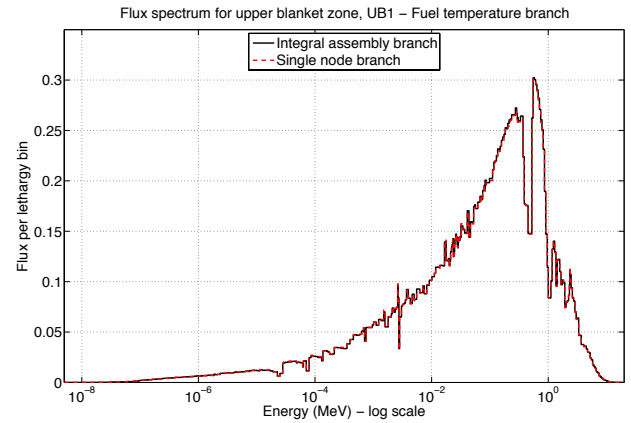


Figure B.4: Comparison of Spectra for Fuel Temperature Perturbation Methods, Upper Blanket

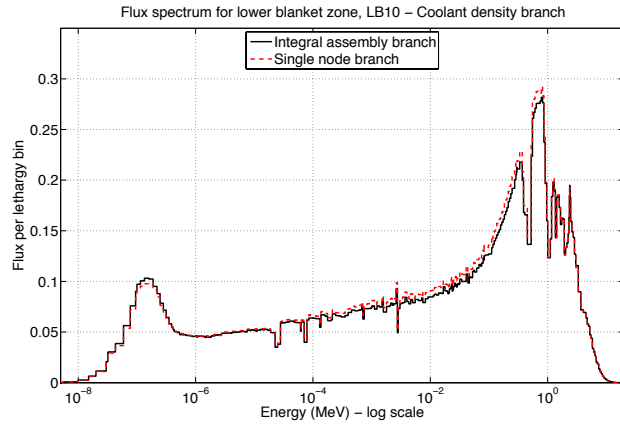


Figure B.5: Comparison of Spectra for Coolant Density Perturbation Methods, Lower Blanket

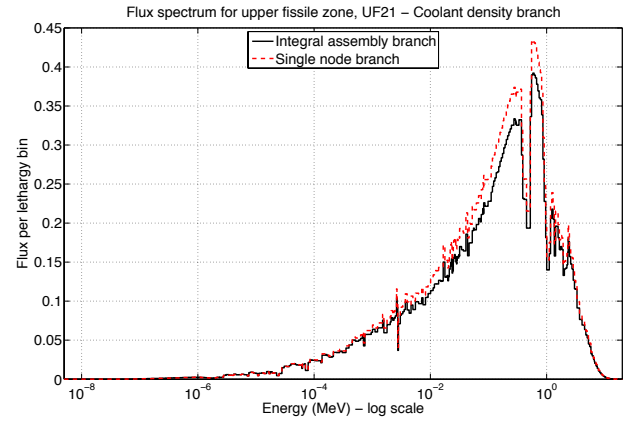


Figure B.7: Comparison of Spectra for Coolant Density Perturbation Methods, Upper Fissile

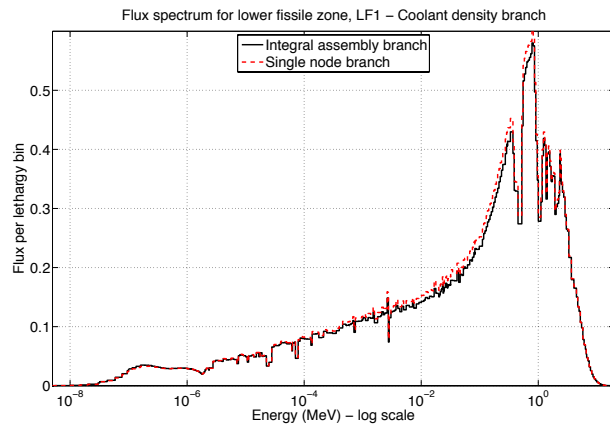


Figure B.6: Comparison of Spectra for Coolant Density Perturbation Methods, Lower Fissile

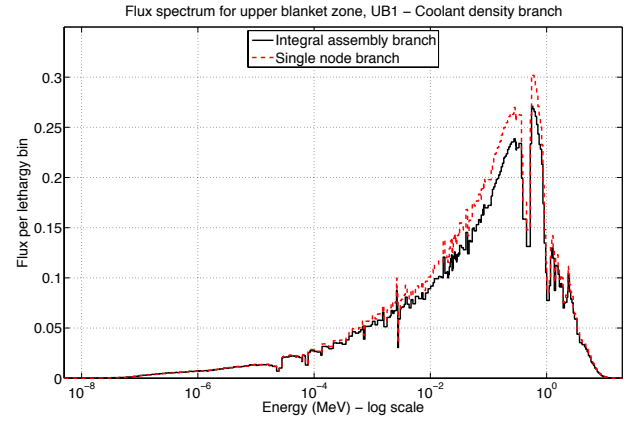


Figure B.8: Comparison of Spectra for Coolant Density Perturbation Methods, Upper Blanket